Contributions in Computer Assisted Diagnosis: Breast Cancer and Autoimmune Diseases

Praful Agrawal

IIITD-MTech-CS-PHD-11-004
April 6, 2014

Indraprastha Institute of Information Technology
New Delhi

Advisors
Mayank Vatsa
Richa Singh

Submitted in partial fulfillment of the requirements
for the Degree of M.Tech. in Computer Science and Engineering

Keywords: Mammography, Saliency, Autoimmunity, Connective Tissue Diseases, Breast Cancer, Indirect Immunofluorescence, and Laws Texture Features.

Certificate

This is to certify that the thesis titled **"Contributions in Computer Assisted Diagnosis: Breast Cancer and Autoimmune Diseases"** submitted by **Praful Agrawal** for the partial fulfillment of the requirements for the degree of *Master of Technology* in *Computer Science & Engineering* is a record of the bonafide work carried out by him under our guidance and supervision in the Image Analysis and Biometrics group at Indraprastha Institute of Information Technology, Delhi. This work has not been submitted anywhere else for the reward of any other degree.

Dr. Mayank Vatsa and Dr. Richa Singh
Indraprastha Institute of Information Technology, New Delhi

Abstract

With the advent of research, it has been established that many leading diseases among women, such as breast cancer, cervical cancer, and autoimmune diseases, can be prevented if diagnosed at initial stage. This research aims at development and analysis of computer assisted systems for accurate diagnosis of such diseases. Among various diseases, this thesis focus upon developing automated systems for screening breast cancer and autoimmune diseases.

Significant research efforts are being made to detect breast cancer symptoms on screening mammograms, however, mass detection has been the most challenging task. The complexity of the task is attributed to varying shape and size of masses and presence of artifacts and pectoral muscles. In this research, we pursue the idea of visual saliency and propose a novel framework to detect mass(es) from screening mammogram(s). The concept of visual saliency is based properties of human vision, therefore, it may help in performing the ”intuitive” tasks which human eye perform with ease such as finding the region of interest. We use the saliency algorithm to segment candidate regions which may contain masses. The qualitative analysis shows that saliency algorithm is capable of detecting mass containing regions without any prior segmentation of pectoral muscles. Extensive feature analysis is performed to obtain the optimal set of features to detect masses using Support Vector Machine based classification. Experiments are conducted on publicly available MIAS database using existing protocols. Results from the comparative analysis show that the proposed framework outperforms the state-of-art algorithms.

Identification of antigen patterns from HEp-2 cells is crucial for the diagnosis of autoimmune diseases. The manual inspection under microscope as well as computer screens is prone to inter-observer variability and lack of standardization. Therefore, efforts are being made to automate the antigen pattern classification from HEp-2 cell images. In this research, we propose a feature categorization to analyze the existing research associated with HEp-2 cell image classification. We also propose an efficient classification system for antigen pattern identification based on Laws texture features. Experiments are conducted using public datasets and existing protocols. Comparison with state-of-the-art techniques clearly indicate that Laws texture features are more efficient for the given task.

Acknowledgments

Towards the completion of my Masters degree, I would like to pay my heartily tributes to people who contributed in many ways. Many companions have witnessed my tough as well as cherishing moments throughout the span of two and half years in IIIT-Delhi. This dissertation is only a part of learning and enormous experience achieved in due course.

After expressing gratitude towards God and my loving parents, I would like to thank my advisors Dr. Mayank Vatsa and Dr. Richa Singh for their support and guidance throughout the journey. Their constant guidance and inputs have helped me prosper towards a more confident and improved personality. They made best of their efforts in supporting me through various possible ways. Their advise has always served me gain more knowledge and selecting better options. I would like to thank my undergraduate advisor Prof. Sanjay Goel, his remarkable vision and kind guidance has been and will remain a constant source of motivation. Also, I would like to thank Dr. Rahul Purandare, Dr. Debajyoti Bera, and Dr. Gaurav Gupta for giving me the cherishable moments at IIIT-Delhi.

I would like to acknowledge the organizers of MIAS and DDSM databases as well as the HEp-2 cell databases - MIVIA and ICIP 2013 cell competition. The present dissertation could not have been possible without the public databases being swiftly available for research. I thank and dearly appreciate the researchers releasing their databases for research purpose.

Other than my parents, my brother has always been a constant companion with unconditional love and support for which any expression of thanks does not suffice. I would like to give special mention to Shruti for being there as a constant source of inspiration and motivating me in the worst as well as best times of my life. I would also like to thank all my friends and companions from IIIT-Delhi who have made my stay dearly memorable and cherishable especially, Denzil, Damodaram, Himanshu, Shiva, Paridhi, Anupama, Monika, Dipto, Ankita, Aditi, Kuldeep, Pandarasamy, Trasha, Anuj, Tejas, Anush, and Ayushi. This section can not be complete without a vote of thanks to the staff at IIIT-Delhi which has always been very helpful in many ways. In the end, I would like to once again thank the Almighty for adding this wonderful chapter to my life.

Dissemination of Research Results

1. AGRAWAL, P., VATSA, M., AND SINGH, R. HEp-2 cell image classification - A computational review. *Under Review.*

2. AGRAWAL, P., VATSA, M., AND SINGH, R. Saliency based mass detection from screening mammograms. *Signal Processing 99*, (2014), 29-47.

3. AGRAWAL, P., VATSA, M., AND SINGH, R. HEp-2 Cell Image Classification: A Comparative Analysis. In *Machine Learning in Medical Imaging* (2013), pp. 195-202.

Contents

List of Figures

List of Tables

Chapter 1

Introduction

1.1 Introduction

According to 2013 report by World Health Organization (WHO) [1], worldwide leading causes of death include cancer, cardiovascular diseases, diabetes, and chronic respiratory disorders. Table 1.1 presents recently published statistics on age standardized adult mortality rate by causes in the year 2008. During recent decades, diagnosis of these diseases heavily depend on the medical imaging technologies such as X-Ray scan, Magnetic Resonance Imaging (MRI), Computed Axial Tomography (CAT), Intra-Vascular Ultra Sound (IVUS), Ultrasonography (USG), Electrocardiography (ECG), and microscopic imaging. These image based techniques are being used during various phases of treatment, starting from early screening to advanced surgery. Such an advent in medical technology is helping clinicians in accurate diagnosis and conducting efficient treatments.

Table 1.1: Age standardized adult mortality rate by cause during 2008 as published in WHO 2013 report [1]. The numbers reported are per 100,000 population in the corresponding regions for people with ages 30-70 years. Minimum, median, and maximum values are also reported as observed from data for all WHO member nations.

Region	**All causes**	**Cancer**	**Cardiovascular diseases and diabetes**	**Chronic respiratory conditions**
African Region	1716	147	382	92
Region of the Americas	532	136	169	24
South-East Asia Region	987	125	322	109
European Region	626	166	238	17
Eastern Mediterranean Region	881	127	344	46
Western Pacific Region	545	168	184	41
India	1002	108	328	133
Global	764	150	245	52
Minimum	220	59	59	2
Median	774	140	284	29
Maximum	3147	284	1427	195

Experts have suggested that some of the incurable diseases, such as breast cancer and cervical cancer, can be prevented if detected at initial stages [80]. WHO has suggested screening programs primarily based on medical imaging technologies to prevent large number of deaths caused due to such diseases. In addition, routine screening is recommended for diseases with high prevalence. Screening programmes have been found effective in reducing the mortality rates by 30% [16]. Generally, during a screening test, an image of internal body part is captured and the aim is to find any symptoms which may indicate prospective incidence of the disease. These medical images are examined by experts and diagnosis is suggested based on the findings from the captured images. With increasing number of screening and diagnostic tests based on imaging technologies, abundant number of medical images are being captured. Since the examination of these images is crucial for the diagnosis, there are important issues to be addressed:

- There is an amount of subjectivity associated with the findings reported by the examining expert. It has been found that two different experts can suggest different findings from a common sample image. This mismatch in opinion is essentially due to the difference in their level of expertise and lack of adequate experience required for accurate examination of medical images [6].
- A large number of images being captured requires a number of human experts. Even in most developed economies such as USA and Europe, the number of available experts is significantly lower. Therefore, in most of the laboratories, experts have to examine large number of samples on daily basis which may affect the overall diagnosis. Table 1.2 presents the number of physicians including specialist physicians as well as general physicians and the data on corresponding essential health infrastructure available worldwide.

Table 1.2: World statistics on physicians (including specialist and general physicians) as well the necessary infrastructure to conduct image based diagnosis in corresponding regions [1]. Minimum, median, and maximum values are also reported as observed from data for all WHO member nations.

Region	**Physicians per 10,000 population (2005-2012)**	**Computed tomography units per 1,000,000 population (2010)**	**Radiotherapy units per 1,000,000 population (2010)**
African Region	2.5	0.4	0.1
Region of the Americas	20.4	NA	5.4
South-East Asia Region	5.5	NA	0.3
European Region	33.3	NA	4
Eastern Mediterranean Region	10.8	1.9	0.3
Western Pacific Region	15.2	NA	1.6
India	6.5	NA	0.4
Global	13.9	NA	1.8
Minimum	0.1	<0.05	<0.05
Median	14.2	3.8	0.7
Maximum	70.6	141.2	28.2

1.2 Medical Image Analysis for Screening and Diagnostic Purposes

Efforts are being made to evolve the computer aided systems for screening and diagnostic purposes. Such systems would eradicate the subjectivity in reported findings and fasten the treatment process. Researchers have been trying to develop the automatized procedures using the tools from computer vision, pattern recognition and machine learning [25], [40]. Other than automation of image interpretation, significant research has been done to develop robotic tools to automate the complex and time consuming tasks in diagnosis. The computer based image analysis systems in combination with robotic tools are also being used during several operated surgeries. Largely, automated procedures in medical diagnosis are dependent on accurate image based techniques. The usefulness of image analysis in different stages of medical treatment process can be categorized as:

- **Enhancement:** Medical images are captured by large cameras which require multiple mechanical calibrations for an accurate and clear image capture. However, due to various practical purposes, most of the times the resultant image contains noise such as out of focus and salt and pepper noise. Therefore, the medical images are required to be processed with a set of image processing techniques to enhance or restore the image for meaningful interpretation and diagnosis.

- **Segmentation:** Medical images are generally captured for diagnosis of a specific organ or region, however, the viewpoint of a sophisticated camera system should be able to capture larger area. Therefore, it is seldom required to carve out the organ or area of interest from captured images. In a manual inspection, doctors are aware of the region of interest and human eyes are capable of easily segmenting the required region. However, in case of automated analysis, segmentation of region of interest is one among the most complex tasks especially due to the surrounding tissues which collude with the delineating boundary. Sophisticated algorithms based on image processing and computer vision are being developed to segment the region of interest from medical images.

- **Registration:** Nowadays, complicated surgeries are being conducted under the purview of sophisticated camera systems where sometimes a tiny camera is inserted into the human body to estimate the ongoing process. In many other cases, multiple cameras are utilized to obtain the internal images. In all such cases, images are simulated and registered with respect to an atlas model. Image processing and linear algebra based techniques have been developed to accurately align the captured images with the existing model. In case of computer assisted surgeries, accurate estimation of the position of inserted tools with respect to the organ is important for a successful surgery.

- **Visualization:** With emerging technologies, more complex image modalities are being used for diagnosis such as Functional Magnetic Resonance Imaging, Photoacoustic imaging, Echocardiography, and Functional Near Infrared Spectroscopy. Such complex images have immense information to be observed and analyzed by doctors to suggest conclusive diagnosis. Therefore, in order to present the highly complex information visualization algorithms are developed. These algorithms project the high dimensionality image on to a computer screen for better visualization as well as they may also indicate important regions to be investigated. Visualization algorithms are also crucial in projecting the run time images captured during computer assisted surgeries.

- **Fusion:** In current scenario, images from multiple modalities are required to diagnose complex diseases. Images captured using various technologies help doctors understand different aspects of the symptoms. Since these images convey different information, they are examined independently, and seldom required to model the complete information. Therefore, image fusion algorithms are being developed to combine the information from different modality images.

- **Storage:** Large number of medical images are being captured for diagnosis in several ways. It is essential to store this humongous data for several important purposes such as to conduct research, to demonstrate important findings to trainees and inexperienced doctors, to assess the impact of treatment and to provide a follow up diagnosis based on historical data. However, two important issues need to be addressed while storing such a valuable data: vast storage space required to save the data, variable formats and the security of data. In order to efficiently store large medical issues, lossless image compression techniques have been developed. Also, a meta data based image format DICOM (Digital Imaging and Communications in Medicine)[1] has been standardized to bring images of different modalities to a common structure. This standardization is also helpful in communicating different modality images across hospitals. The security of medical information is crucial as it may contain sensitive personal information. Therefore, watermarking techniques are being utilized to encode the identity of patient to make it accessible only to legitimate users.

In order to develop efficient computer based models, tools from pattern recognition and machine learning are also required. Most of the automated systems rely on combination of image processing and decision making techniques to suggest a meaningful diagnosis. Such systems being used at several stages of medical treatment has motivated researchers to develop efficient techniques. The proposed techniques need to be thoroughly evaluated on existing data in order to establish their clinical utility. As a result, most of the exciting research being conducted is validated and thoroughly evaluated by existing benchmarks and public datasets.

1.3 Research Contributions

Worldwide, leading causes of death among women include breast cancer, cervical cancer, autoimmune diseases, arthritis, anemia, heart disease, and osteoporosis. Efforts are being made to generate awareness among women to consult physicians as soon as they experience any symptoms. Moreover, screening programs have been started by various countries to detect most prevalent diseases such as breast cancer and cervical cancer. Though such programs are essential and have proven to be effective, they still require human experts to analyze the image based medical data and propose a relevant diagnosis. Therefore, computer based detection/diagnosis systems are being developed to automate the role of human experts.

In this thesis, we focus on two aspects: breast cancer screening and diagnosis using mammograms and HEp-2 (human epithelial type 2) cell classification. The research contributions in this thesis can be summarized as:

[1] http://dicom.nema.org/

- Screening mammography has been successful in early detection of breast cancer, which has been one of the leading causes of death for women worldwide. Among commonly detected symptoms on mammograms, mass detection is a challenging problem as the task is affected by high complexity of breast tissues, presence of pectoral muscles as well as varying shape and size of masses. In this research, a novel framework is proposed which automatically detects mass(es) from mammogram(s) even in the presence of pectoral muscles. The framework uses saliency based segmentation which does not require removal of pectoral muscles, if present. From segmented regions, different features are extracted followed by Support Vector Machine classification for mass detection. The experiments are performed using an existing experimental protocol on the MIAS database and the results show that the proposed framework with saliency based region segmentation outperforms the state-of-art algorithms.

- Indirect Immunofluorescence (IIF) testing is the state-of-art procedure to detect antinuclear autoantibodies. However, due to lower level of standardization and automation, large number of experts are required to analyze the test images. In this research, we focus on automated identification of antigen patterns from HEp-2 cell images. Recently, many techniques have been proposed to automate this task. We propose a feature categorization based on different object properties and analyze the existing literature based on this categorization. We also propose to utilize Laws texture features for the HEp-2 cell image classification. Experimental analysis is performed to evaluate and compare the performance of Laws texture features with other widely used image based features. Comparative results on two public datasets using different protocols conclude that Laws texture features are efficient for the given task.

Chapters 2 and 3 present the proposed computer aided systems to automate the diagnosis of breast cancer and autoimmune diseases respectively using image interpretation and decision making algorithms. Finally, Chapter 4 summarizes the contributions of the thesis with discussion on possible future research directions.

Chapter 2

Saliency based mass detection from screening mammograms

2.1 Introduction

For the past few decades, cancer has been a major cause of deaths worldwide. World Health Organization (WHO) has predicted that the number of deaths due to cancer will increase by 45% from 2007 to 2030. In 2030, new cases of cancer are expected to reach 15.5 million from 11.3 million reported in 2007[1]. Detailed statistics from WHO show that breast cancer accounts for the maximum number of newly reported cases and deaths caused due to cancer among women worldwide. The symptoms of breast cancer can be detected with the help of X-ray of breasts, termed as *mammograms*. Experts have suggested that the best possible cure for breast cancer is the early prognosis of these symptoms.

With increasing awareness about the disease, thousands of mammograms are captured annually in the screening centers. Even in most of the developed economies such as USA and Europe, there is a mismatch between the number of experts available and the number that is required to analyze the screening mammograms. Due to the lack of medical experts required to analyze the screening mammograms, scientists have realized the role of Computer Aided Detection/Diagnosis systems to automate the diagnosis of screening mammograms. Computer Aided Detection systems (CADe) are used to detect early symptoms from medical images and Computer Aided Diagnosis systems (CADx) are used to diagnose abnormal findings. Some studies [4], [13], [14] claim that the use of CAD systems has actually improved the diagnosis of breast cancer, however other experiments [76] do not agree with these results. Amid such varied results, scientists emphasize on using CAD systems as secondary opinion for doctors.

For breast cancer prognosis, a CADe system detects early symptoms from screening mammograms. As shown in Figure 2.1, the commonly detected symptoms on mammograms include

- clustered micro-calcification,
- mass,

[1] `http://www.who.int/features/qa/15/en/index.html`, last accessed on June 12, 2013.

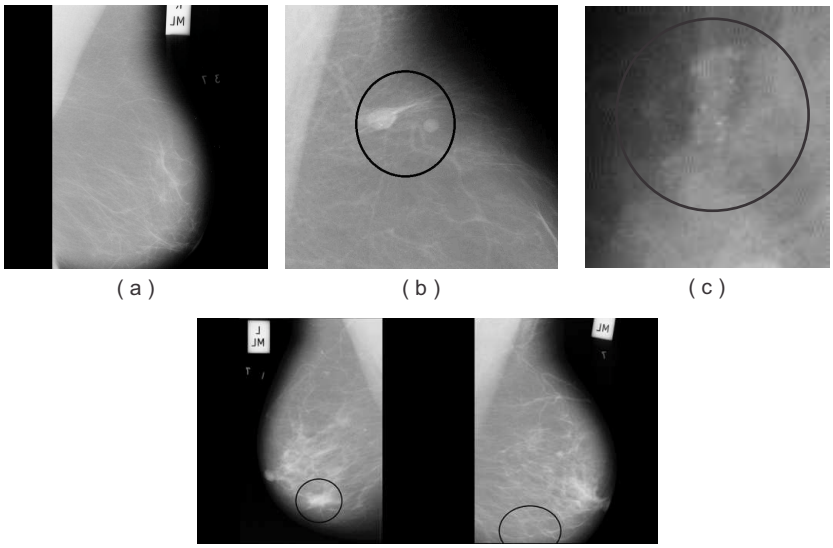

Figure 2.1: Sample images: (a) normal mammogram, (b) cluster of micro-calcification, (c) a part of mammogram containing mass, and (d) left and right mammograms of the same patient showing a case of bilateral asymmetry. Source: MIAS Database [92].

- architectural distortion, and
- bilateral asymmetry.

Clustered micro-calcification is a very prominent symptom observed in new cases of breast cancer. As illustrated in Figure 2.1, they appear as a group of white dots on a mammogram. A mass is defined as a space-occupying lesion seen in more than one projection [93]. They vary in size and shape [71], and therefore are difficult to detect in mammograms. Figure 2.1 illustrates a case with cancerous mass present in a mammogram. Architectural distortion and bilateral asymmetry are not very common symptoms and multiple images are required to detect these symptoms. For example, architectural distortion can be detected by comparing the screening mammograms captured before and after the distortion is developed. Bilateral asymmetry corresponds to any significant difference in the tissue structure between the two breasts (left and right). Figure 2.1 shows a sample case of bilateral asymmetry.

Mammograms are generally captured from multiple views to collect as much information as possible before detection/diagnosis. Some widely captured views are Carnio-caudal (CC) and Multi-lateral Oblique (MLO). A CC view mammogram is taken from above a horizontally-compressed breast and shows as much as possible of the glandular tissue, the surrounding fatty tissue, and the outermost edge of the chest muscle. On the other hand, a MLO view mammogram is captured from the side at an angle of a diagonally compressed breast thus allowing more of the breast tissue to be imaged as compared to other views. However, with this procedure, pectoral muscles also appear in MLO view mammograms. As shown in Figure 2.2, these pectoral muscles have high intensity values in the mammogram and may be misinterpreted as mass. Therefore, algorithms generally involve removing the pectoral muscles or a segmentation step to suppress pectoral muscle region followed by detection of symptoms. Even with the

availability of multiple views, only few automatic mammogram analysis algorithms combine information and perform case based analysis using multiple views simultaneously [98]. Most of the algorithms consider and process each view as an individual image.

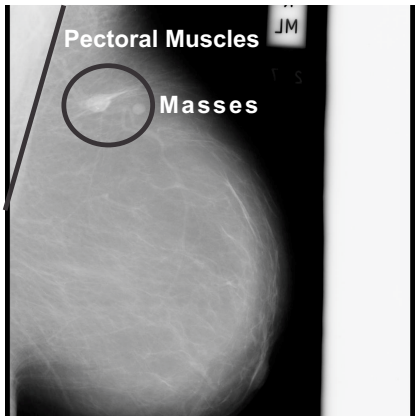

Figure 2.2: Pectoral muscles indicated on a MLO view mammogram containing masses.

Many sophisticated algorithms have been proposed to detect the symptoms from screening mammograms [37], [79], [80]. As shown in Figure 2.1, there are multiple symptoms of breast cancer. While efficient algorithms for detection and diagnosis of micro-calcification exist [42], the same is not true for masses [86]. Detection and diagnosis of masses in a mammogram are challenging problems due to the varying size, shape, and appearance of masses as well as varying tissue density (Figure 2.3). Detection and diagnosis corresponds to two different stages of the complete diagnosis. Detection refers to finding the possible location(s) of mass in the complete mammogram, while diagnosis is the final step of finding the exact boundaries of the mass present and/or classify the segmented mass as benign or malignant [71]. Even though there are algorithms that can address both the problems simultaneously, researchers generally try to solve them independently. Successful detection is crucial for meaningful diagnosis and therefore, in this research, we focus on mass detection from screening mammograms.

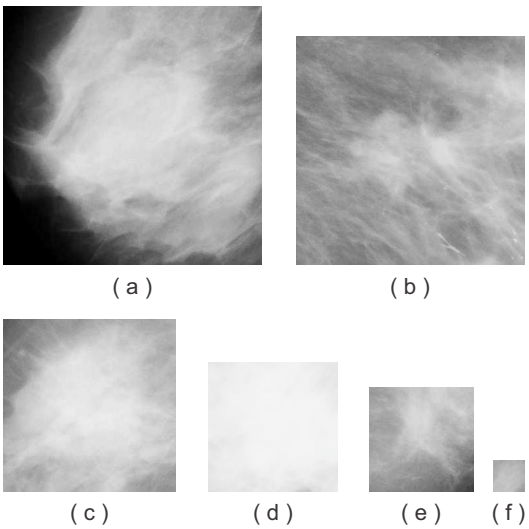

Figure 2.3: Sample of mass regions from the MIAS database [92].

2.1.1 Literature Review

In literature, several researchers have proposed algorithms to detect masses in mammograms. Table 2.1 summarizes some of the key contributions for mass detection. Vyborny and Giger [99] discussed the algorithms to detect abnormalities such as mass and micro-calcification from mammograms using CAD systems. They concluded that for a fair comparison, the algorithms should be evaluated on a public database. However, in the absence of any such database, existing algorithms compare their results directly with the radiologist's assessment. In the same year, Mammographic Image Analysis Society [92] released a public database comprising 322 digitally scanned film based mammograms. Later, another database known as the Digital Database for Screening Mammography (DDSM) [45] was published for research purpose. These databases and few others have helped the researchers to identify and solve some key problems associated with the development of CAD systems for screening mammograms. Cheng *et al.* [20] summarized the existing algorithms for one of the key challenges in screening mammograms i.e, detection and classification of masses. They discussed the various steps involved in an automated approach and the key processing algorithms proposed in literature for modeling these steps. They also compared the results of different classifiers with radiologist's performance on the Nijmegen and DDSM databases. Tang *et al.* [93] analyzed the advent of CAD systems using mammography in a more generic way and focused on computer aided detection of four major symptoms in screening mammograms. A categorical review of existing algorithms was presented and the authors suggested that CAD systems could assist radiologists in validating their assessment. They also suggested that further improvement is required if such systems are to be used in an independent manner. Oliver *et al.* [71], in their recent survey, analyzed existing algorithms according to various computer vision paradigms used for segmentation of suspicious regions and the features used to model the variations in normal and cancerous tissue patterns. They also compared seven key mass detection approaches on a common set of images using one experimental protocol and observed that in general, the performance varies with shape and size of masses as well as with the density of breast tissues.

Table 2.1: Summary of key existing techniques for mass detection.

Technique	**Description**	**Database**	**Results**
Lai *et al.* [58] 1989	Adaptive thresholding is used to detect suspicious regions from enhanced image. Template matching is used to identify masses from candidate regions.	Training: 7 images with 11 masses. Testing: 17 images with 19 masses.	100% TP @ 1.1 FP/image.
Petrick *et al.* [75] 1996	Edge detection is applied to find the boundary of the objects highlighted in DCWE filtered image. Morphological features are used to classify objects as mass or non-mass.	25 images containing one mass each.	96% TP @ 4.5 FP/image.

Continued on next page

Table 2.1 – continued from previous page

Technique	Description	Database	Results
Karssemeijer *et al.* [53] 1996	Pixel orientation map is obtained with the help of three dimensional second order Gaussian derivative operators. Orientations at a scale with maximum response of Gaussian operators are selected for further processing. Two statistical features are computed from the orientation map to detect stellate patterns.	31 normal breast images, 9 images with malignant stellate lesions and 10 images with architectural distortions are used from MIAS database.	90% TP @ 1 FP/image.
Polakowski *et al.* [77] 1997	Difference of Gaussian smoothed images followed by thresholding is used to segment Regions of Interest (ROI) from pre-processed image. Texture features based classification is used to classify segmented ROI as mass or non-mass.	Total 272 images used with 36 malignant and 53 benign cases.	92% accuracy for locating masses. 100% TP @ 1.8 FP/image.
Eltonsy *et al.* [28] 2007	Multiple concentric layer model is designed to detect the suspicious regions in a mammogram. Minimum distance between two segmented regions and probability of presence of a suspicious region in the given mammogram are used to reduce the false accepts.	Training: 135 malignant cases. Testing: 135 malignant, 82 normal and 135 benign cases. All images from DDSM database.	92% TP @ 5.4 and 5 FP/image respectively for malignant and normal cases, 61.6% TP @ 5.1 FP/image for benign cases.
Kom *et al.* [54] 2007	Image enhanced by linear filter is subtracted from original image to obtain the suspicious regions. Local Adaptive Thresholding is applied to the subtracted image to obtain the detected masses.	34 images containing 49 lesions and 27 normal images used.	95.91% TP @ 15% FPR.
Varela *et al.* [97] 2007	Iris filter is applied in a multiscale fashion followed by adaptive thresholding is used to segment the suspicious regions. Gray level, texture, contour, and morphological features are used for classification.	66 malignant and 49 normal cases used with 4 images per case.	88% and 94% TP @ 1.02 FP/image for per image and per case evaluation respectively.

Continued on next page

Table 2.1 – continued from previous page

Technique	Description	Database	Results
Hong and Sohn [50] 2010	Suspicious regions are modeled with the help of a topographic representation termed as isocontour maps. A hierarchial representation, inclusion tree is used to capture the relationship between contours and minimum nesting depth is used to identify the masses.	400 images selected from DDSM database.	100% TP @ 3.8 FP/image.
Gao *et al.* [39] 2010	Combination of Morphological Component Analysis (MCA) and Concentric Layer Model is used for mass detection.	Training: 40 malignant and 10 benign cases. Testing: 100 malignant and 50 benign cases. All images from DDSM database.	99% TP @ 2.7 FP/image for malignant cases and 88% TP @ 3.1 FP/image for benign cases.
Mencattini *et al.* [65] 2010	Suspicious regions are detected based on measure of convergence of gradient vectors in a circle from center pixel in a pre-processed image. Parametric thresholding is used as false positive reduction.	136 images selected from DDSM database containing one mass each.	100% TP @ 5 FP/image.
Sampaio *et al.* [8] 2011	Cellular Neural Networks are used to detect the suspicious regions in a pre-processed image. Texture features derived from geostatic functions and shape features are used for classification.	623 images randomly selected from DDSM database.	80% TP @ 0.84 FP/image.

Some commercial systems such as ImageChecker CAD[2] and SecondLook Digital[3] are also available and are nearly accurate in detecting micro-calcifications, however the accuracies of mass detection require improvement [86]. Based on our observation, following are the key challenges in designing an efficient mass detection algorithm:

- Existing databases consist of noisy mammograms. Noise in mammograms is mainly due to the old film based X-rays, such as mechanical noise in the image background and certain irregularities such as tape markings and occlusions. Therefore, mammogram analysis starts with an overhead step of image cleaning, which generally involves masking out the breast region. However, this

[2] `http://www.hologic.com/en/imagechecker-cad`, last accessed on June 12, 2013.

[3] `http://www.icadmed.com/products/mammography/secondlookdigital.htm`, last accessed on June 12, 2013.

masking disrupts the natural texture on the outer boundary of breast region thereby creating a hard edge. Such hard edges can easily confuse the segmentation algorithms. In order to develop more useful and efficient algorithms, such unwanted hard edges on the breast boundary must be diluted before segmentation.

- In mass detection algorithms, pectoral muscle segmentation is an important step as the presence of pectoral muscles may increase false alarms generated by automatic segmentation algorithms [38]. Though several researchers have proposed dedicated pectoral muscle segmentation algorithms [12], [31], [38], [57], [67], it is still challenging to accurately segment these muscles when the tissue density around the muscles is high. Therefore, it is important to design more robust algorithms that do not require segmenting the pectoral muscle boundaries.

- False positive reduction is used to remove the falsely segmented regions. Existing algorithms consider the segmented Regions of Interest (ROI) as a single entity for the false positive reduction step. Very often these regions contain mass surrounded by normal tissue regions or mass present in different orientations. Such regions can lead to ambiguity in feature values and therefore reduce the performance.

- Features are generally derived from the properties of objects present in an image such as texture, shape, gradient, and intensity. Many such features have been proposed/used for mass detection [20], [71]. However, only subsets of these features have been used by researchers repeatedly. There is no study that analyzes a comprehensive feature space in a common framework and determine their effectiveness.

2.1.2 Research Contribution

In this research, a framework for mass detection from mammograms is proposed which attempts to answer the key issues in existing approaches as identified in the previous subsection.

- The pre-processing step in the proposed framework utilizes image blending to diffuse the hard edges formed due to masking.

- *Visual saliency* is proposed to segment probable mass containing regions in a pre-processed mammogram. One of the key findings of the study is that the saliency based segmentation is robust to the presence of pectoral muscles.

- For improved mass detection, candidate regions obtained from visual saliency based segmentation are examined. A grid based approach is utilized to examine the regions of interest and different features are extracted, analyzed, and compared individually. Further, feature selection and dimensionality reduction algorithms are investigated to obtain the optimal set of features. Using the protocol of Oliver et al. [71] on the MIAS database, classification results show that the proposed algorithm yields better performance than existing algorithms.

2.2 Proposed Framework for Mass Detection

In this research, a framework for detection of masses from screening mammograms is proposed. The proposed framework uses visual saliency based segmentation and a set of optimal features to detect mass in screening mammograms. Figure 2.4 illustrates the steps involved in the proposed framework - pre-processing, ROI segmentation, grid based sampling of ROI, feature extraction, and classification.

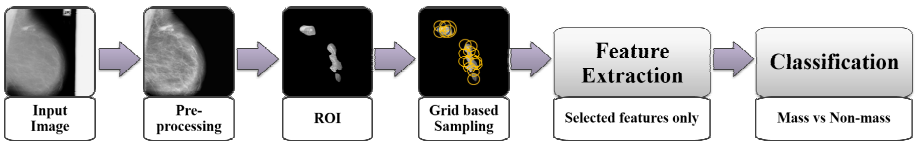

Figure 2.4: Illustrating the steps involved in the proposed framework.

2.2.1 Pre-processing

The mammogram images are generally low on contrast and have noise in background such as tape markings and labels (as shown in Figure 2.5) which may affect the segmentation results. Therefore, contrast enhancement and background segmentation are crucial pre-processing steps for a CAD system to analyze mammograms [56], [81], [88]. In this research, a set of completely automated pre-processing steps are used to remove the background noise and enhance the image quality of mammogram images. The pre-processing steps illustrated in Figure 2.6 are,

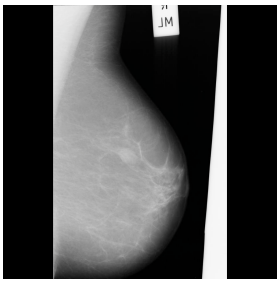

Figure 2.5: Low contrast mammogram with occlusion and noisy background.

- **Masking:** The first step of pre-processing estimates the breast boundary using a gradient based approach proposed by Kus and Karagoz [56]. Adaptive global thresholding followed by histogram stretching are used to compute the outline of breast region and generate the mask. To ensure that any breast region is not missed, the mask is dilated using a circular structuring element of pixel size five. Finally, the dilated mask, as shown in Figure 2.6, is used to remove the background noise.

- **Enhancement:** In literature, several contrast enhancement techniques have been proposed for the enhancement of mammograms [88]. In this research, adaptive histogram equalization is applied to enhance the contrast of masked mammogram image [41]. Figure 2.6 shows the contrast enhanced image thus obtained.

- **Blending:** In masking, the background region pixels are assigned zero intensity, which creates hard edge along the border of the segmented region. This artificial hard edge leads to undue saliency accumulation along the border. Therefore, we utilize the concept of image blending to dissolve the hard edges. Gaussian-Laplacian pyramid [15] based image blending is used to blend the masked image with the original image only along the outer breast boundary. The two images are decimated into a Gaussian- Laplacian Pyramid upto seven levels. Blending is applied at each level of the pyramid and finally the image is reconstructed.

- **Cropping:** Though image blending removes the hard edges at the outer boundary, it fails to dissolve the thick vertical edge on one side of the mammogram. Such edges are obtained when the breast region lies in the middle of the image; an example is shown in Figure 2.7. To address this issue, as shown in Figure 2.7, image is cropped such that the breast region is aligned to its respective sides.

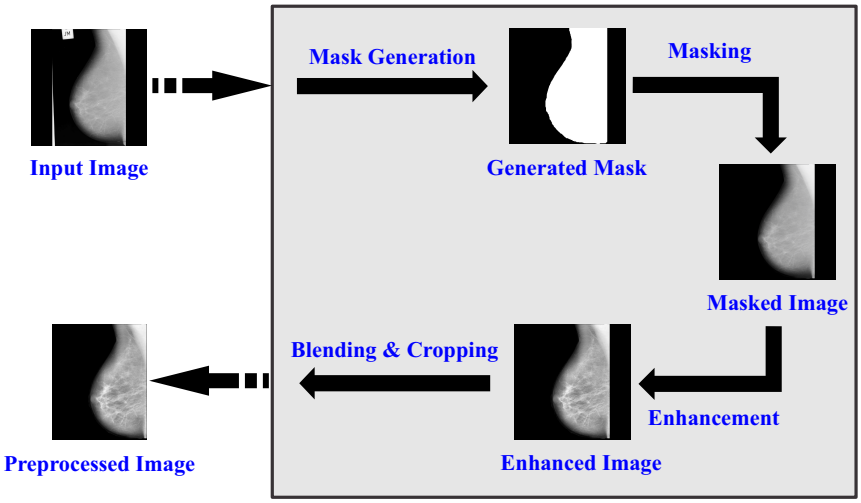

Figure 2.6: Steps involved in pre-processing of mammograms.

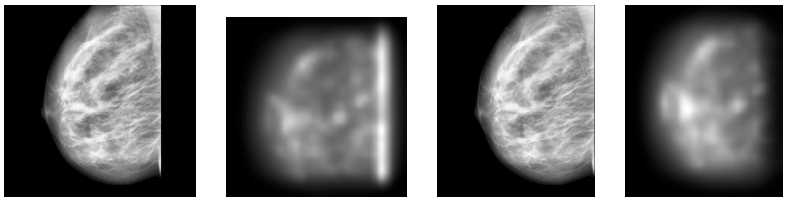

Figure 2.7: (a) Enhanced image without cropping, (b) saliency map without cropping, (c) enhanced image after cropping, and (d) saliency map pertaining to cropped and enhanced image.

2.2.2 Saliency based ROI Segmentation

After preprocessing, the region of interest (region where mass is expected) is to be segmented. The anatomy of breast is a complex structure due to the presence of pectoral muscles as well as the varied

density of breast parenchyma. For an expert, it is easy to analyze breast tissues without getting confused with pectoral muscles. However, for an automatic algorithm, it is difficult to differentiate between pectoral muscles and mass. Therefore, generally, pectoral muscles are removed before segmenting the ROI. Automatic pectoral muscle segmentation is a difficult task, and it is also an overhead in processing the mammograms without pectoral muscles such as Carnio-Caudal (CC) view mammograms. Therefore, in this research, we propose the visual saliency based ROI segmentation in mammograms which does not require the location of pectoral muscles at any time of processing to detect the ROI.

Visual saliency models the ability of humans to perceive salient features in an image. In computer vision, visual saliency models are bottom-up techniques which emphasize on particular image regions such as regions with different characteristics [10]. Visual saliency models can be classified as space-based or object-based models. Object-based models assign higher saliency to the regions containing objects. On the other hand, space-based models produce a saliency map of the input image. It is represented as a probabilistic map of an image where the value at a pixel location corresponds to the saliency of that pixel with respect to the surroundings. It can also be very useful in cases where some structures are implicit with respect to the image such as pectoral muscles in mammograms. A simple visual saliency based segmentation algorithm can be designed by applying thresholding on the saliency map (or probabilistic map).

Several visual saliency based algorithms have been proposed in literature [9], [10]. Since the screening mammograms are gray scale images, algorithms which utilize the multi-channel properties of color images may not be useful. Saliency algorithms which are capable of computing visual saliency from a grayscale image such as Esaliency [2], GBVS [44], Hou and Zhang [51], and Liu *et al.* [63], are considered to segment ROI from the pre-processed mammogram. Any of these algorithms can be used for generating saliency maps, however, we experimentally observed that GBVS yields the best results. Therefore, in this research, we use saliency maps generated by GBVS to extract the ROI.

GBVS computes saliency of a region with respect to its local neighbourhood using the directional contrast. Saliency computation is directly correlated with the feature map used. In screening mammograms, it has been observed that the contrast of mass containing regions is significantly different from the remaining breast parenchyma. As discussed earlier, mass surrounded by dense tissues are tough to detect, however, the directional contrast with respect to the local neighbourhood helps in identifying such masses along with the masses present in fatty regions. It is to be noted that the fatty regions surrounded by dense tissues may also get falsely detected, such regions are discarded at the final classification stage. The steps involved in computing the saliency map are explained below[4].

1. Mass differs in contrast from the neighboring regions, therefore feature maps are computed from contrast values along four different orientations of 2D Gabor filters ($0°$, $45°$, $90°$, and $135°$).

2. The saliency maps can be derived in a naïve way by squaring all the values in the feature map obtained in the previous step. However, this naïve method can result in a large number of falsely detected regions indicated as salient regions. Therefore, activation maps are computed as the

[4]Please refer to the original paper by Harel *et al.* [44] for more details on GBVS algorithm.

equilibrium distribution of ergodic Markov chain [60], obtained using the initial feature maps. The equilibrium distribution will lead to higher weights only for the edges present in salient regions. Moreover, the higher edge weights initialised in regions other than salient regions will get diffused in the equilibrium distribution. Ergodic Markov chains are modeled on a fully connected directed graph obtained from feature maps. The graph is generated by connecting nodes in a feature map using weighted connections. The weight of an edge connecting node (i, j) to node (p, q) in the graph is assigned as,

$$w((i,j),(p,q)) \triangleq D \cdot F(i-p, j-q), \tag{2.1}$$

$$where, F(a,b) \triangleq exp\left(-\frac{a^2+b^2}{2\sigma^2}\right) \tag{2.2}$$

$$D \triangleq \left|log\left(\frac{M(i,j)}{M(p,q)}\right)\right| \tag{2.3}$$

$M(i, j)$ represents a node in the feature map and σ is set to 0.15 times the image width[5].

3. Final step in saliency algorithms is generating saliency map from activation maps. However, in general, some individual activation maps lack accumulation of weights in salient regions, therefore, an additional step of normalization of activation map is performed to avoid uniform saliency maps. GBVS normalize activation maps using a similar approach as used in the previous step, i.e. the equilibrium distribution of ergodic Markov chain to accumulate high activation values in salient regions. Markov chains are obtained from activation maps in a similar manner as discussed in the previous step, however, the function D in Eq. 2.1 now maps to the value at location (p, q) in activation map (Eq. 2.4) and value of the parameter σ in Eq. 2.2 is 0.06 times the image width[5],

$$D \triangleq A(p,q) \tag{2.4}$$

where $A(p, q)$ represents a node in the activation map.

4. Finally, normalized activation maps are combined using sum rule to obtain the saliency map.

Once the saliency map is computed, a threshold equal to half of the maximum value[6] in saliency map is used to obtain the ROI. The regions containing less than 100 pixels are discarded for further analysis. Figure 2.8 illustrates some examples of saliency maps generated from pre-processed images and ROI segmentation from the saliency maps.

2.2.3 Grid based Sampling of ROI

Since GBVS algorithm extracts salient regions in a more generic manner, therefore, along with mass, the segmented regions contain some normal tissues as well. The proposed framework utilizes a grid based search to detect the mass containing regions and discard the falsely detected normal tissue regions.

[5] We empirically found that σ value suits all images in the MIAS database.
[6] Threshold=0.5 is empirically selected to obtain the optimal size ROIs.

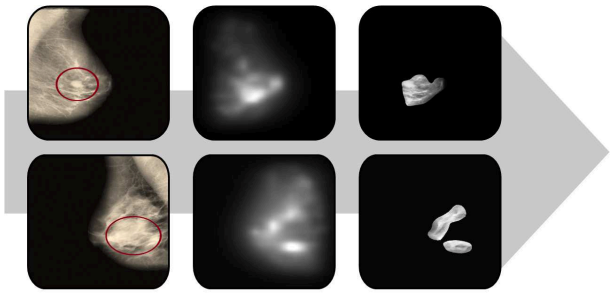

Figure 2.8: Saliency map generated from enhanced image and suspicious regions obtained after thresholding.

Within the bounding box covering the segmented ROI, a grid of seed points is marked with each point marked 40 pixels apart in both horizontal and vertical directions. Overlapping circular regions of radii varying from 30 pixels to 210 pixels are extracted using all the seed points and features are extracted from these regions. The size of circular regions is selected to be varying from 30 pixels to 210 pixels in order to model a generalized approach independent of mass size. Figure 2.9 illustrates an example of extracting circular regions from the segmented ROI.

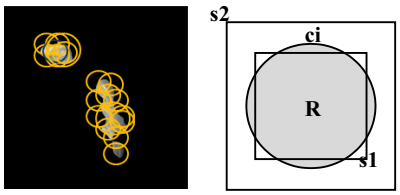

Figure 2.9: (a) Circular regions extracted from ROI and (b) representation of each circle for feature extraction.

2.2.4 Feature Extraction

In this research, we have extracted a large number of features and clustered these features among three different categories namely, Spatial domain features, Fourier domain features, and Wavelet entropy features. The categorization is based on the information used to compute these features. Various features belonging to these three categories have been explored by researchers for discriminating between mass and non-mass regions. However, current literature lacks the understanding of individual features and their combination. One of the key contributions of this research includes analysis of the large pool of features in top-down as well as bottom-up approach to find the optimal set of features. This section further explains the extracted features as well as the feature selection techniques utilized to obtain the relevant feature set.

Fourier Domain Features

Spectral energy features have been used by researchers to differentiate mitotic nuclei from others present in microscopic images of biopsy slides for breast cancer [11]. Fourier domain representation of the pixels in ROI is used to compute the spectral energies which represent the energy in different frequency bands. Spectral energies are calculated from the Fast Fourier Transform (FFT) of one-dimensional signal formed

by the pixels in the ROI, FFT is computed using Eq. 2.5. From this FFT representation, 35 energy values are computed from different frequency bands as explained in Section 5.1.

$$FFT\_ROI = \sum_{n=0}^{N-1} x(n)e^{-j2\pi nk/N}, k = 0, 1, ..., N-1 \tag{2.5}$$

where, $x(n)$ represents the pixels of region R in spatial domain and N represents the total number of pixels in region R.

Wavelet Entropy Features

In some cases, the masses may be surrounded with highly dense tissues along different directions. Discrete Wavelet Transform (DWT) encodes the details present in an image along different directions. Wang *et al.* [100] has shown that entropy features computed in wavelet domain can efficiently differentiate between the masses and normal breast tissues. Nine features encoding the entropy of upto three level DWT detailed sub-bands are extracted from the circular regions. As the ROI size is much smaller compared to the complete mammogram, meaningful decimation can be upto level three only. Beyond level three, the smaller sized masses remain for few pixels only. On the other hand, Redundant Discrete Wavelet Transform (RDWT) [33] is undecimated, therefore it can be used to extract the entropy information even at higher levels. Here, RDWT upto level four is used to extract the entropy features.

Let I be the mammogram image and I_{Hl}, I_{Vl}, I_{Dl} be the detailed sub-bands at level l representing the horizontal, vertical and diagonal high level coefficients respectively. R_{Hl}, R_{Vl}, and R_{Dl} represent the set of DWT coefficients from the detailed sub-bands I_{Hl}, I_{Vl}, and I_{Dl} respectively mapped to the pixels in region R on a mammogram. Entropy is calculated for each sub-band region as $A_i^l = -\sum p_{il} * log(p_{il})$, where $i = H, V$, and D. A_H^l, A_V^l, and A_D^l represent the entropy of horizontal, vertical and diagonal coefficients respectively at level l from DWT representation and p_{il} represents the normalized histogram of values in R_{il}. In a similar manner, the entropy features are computed from the RDWT sub-bands, $B_i^l = -\sum p_{il} * log(p_{il})$, where $i = H, V, D$ where B_H^l, B_V^l, and B_D^l represent the entropy of horizontal, vertical and diagonal coefficients at level l from RDWT representation respectively.

Spatial Domain Features

The spatial domain features include Laws texture features, intensity features, run-length texture features, and statistical texture features commonly used by existing algorithms [20], [61]. To extract the spatial domain features, let us assume circle ci be the set comprising all the boundary points of ROI, R be the set containing all points in the region of interest, square $s1$ be the square region with area and center same as ci, and region $s2$ be the square with each side exactly five pixels more than $s1$ and center same as ci. This provides us two squares and a circle as shown in Figure 2.9, we now extract five different features from the distribution formed by pixels in these regions.

- *Intensity Features:* It has been observed that the intensity of mass varies with respect to the sur-

rounding tissues. Based on this intuition, researchers have proposed some thresholding based and morphology based algorithms [28], [71], [93]. However, we model this variation with the help of five features computed from the pixel values within and out of the suspicious regions namely, Mean Intensity, Intensity Variation, Mean Intensity Difference, Skewness, and Kurtosis. Detailed information about computing these features is available in Section 5.2.

- *Laws Texture Features:* Laws [59] proposed five linear kernels for texture based segmentation that represent edges, ripples, waves, lines, and spots in a square region as shown in Table 2.2. Polakowski *et al.* [77] studied 25 feature masks generated by the combination of these kernels and found that eight of them are the most discriminating for detecting masses in mammograms. These eight features are used in this experiment to map the texture information present in the segmented regions. Each of these features are computed with the help of feature masks described in Section 5.3. The preprocessed image is convolved with these feature masks and the mean value corresponding to pixel locations in circular regions are considered as feature values.

Table 2.2: Kernels proposed by Laws [59].

Kernel Label	**Kernel Values**
l5	[1 4 6 4 1]
s5	[-1 0 2 0 -1]
e5	[1 -4 6 -4 1]
r5	[-1 -2 0 2 1]
w5	[-1 2 0 -2 1]

- *Statistical Texture Features:* Statistical texture features, also known as Spatial Gray-Level Dependence (SGLD) features, use statistical measures to model the pattern of intensity values in a region [43]. These features have been used by many existing approaches to differentiate between breast tissues as normal or cancerous [20]. The features are computed using the Gray Level Co-occurrence Matrix (GLCM) which quantifies the number of occurrences of gray level i in a spatial relation with gray level j. The image is discretized to eight gray levels and GLCM matrices are obtained for four orientations (0°, 45°, 90°, and 135°). The four GLCM matrices obtained are normalized and 13 features are extracted from each of the four matrices. Section 5.4 contains detailed description of these features. Further, 13 additional features are computed as mean of these individual features.

- *Run Length Texture Features:* Another widely used measure of texture includes features based on the Gray Level Run Length (GLRL) matrix [94]. These features measure the simultaneous presence of intensity values for varying continuous lengths in different directions. GLRL matrix $G(x, y|\theta)$ represents the run length matrix in a given direction θ. These can be helpful in modeling complex textures such as breast tissues and have been used for mass detection in some existing approaches [20]. In total, 20 features are computed from GLRL matrices in four different directions. GLRL matrix for four directions (0°, 45°, 90°, and 135°) are computed and the features derived from these matrices are explained in 5.5.

Feature Selection

154 features are extracted from each circular region. These features are evaluated in the proposed framework resulting in selection of optimal features to discriminate between mass and non-mass regions. The features are analyzed individually as well as in combination using feature selection and dimensionality reduction algorithms. In this research, feature concatenation is used to combine any two feature sets.

Firstly, the performance of all individual set of features is evaluated. Mutual information based feature selection [73] is used to further analyze these feature sets and obtain optimal features out of these individual sets. Features with significant performance are then combined to seek better classification. Mutual information based feature selection [73] uses a minimum Redundancy Maximum Relevance (mRMR) criterion to measure the discrimination power of features. Mutual information between two random variables x and y with probability density functions $p(x)$, $p(y)$ and $p(x, y)$ is computed using Eq. 2.6.

$$MI(x; y) = \int \int p(x, y) log \frac{p(x, y)}{p(x)p(y)} dxdy \tag{2.6}$$

According to the mRMR criteria, optimal features must have high mutual information with the target labels in order to represent the maximum dependency. The theoretical analysis of mRMR based feature selection algorithm is discussed by Peng *et al.* [73]. The mRMR based feature selection arranges the features in decreasing order of their discrimination ability using the input feature values and optimal number of features is obtained by evaluating different number of features selected from top of the list.

Based on the initial results of individual feature sets, a combined set of features is obtained using feature concatenation. The combined set of features is analyzed with the help of mRMR feature selection and Principal Component Analysis (PCA) [3] based dimensionality reduction.

2.2.5 Classification

The features extracted from circular ROIs are classified using a $2-$class SVM with the classes being mass and non-mass. SVM [19] with polynomial kernel of degree three is trained to obtain the decision boundary. The training data for SVM is $\{\overline{x}, y\}$, where $\overline{x}$ represents the feature vector extracted from the circular ROI with training label $y \in \{+1, -1\}$. $+1$ represents the positive (mass) class and -1 represents the negative (non-mass) class. The actual labels of circular ROIs are obtained using the ground truth information available with the database. Any circular ROI is assigned a positive label if the center of the mass is present within the ROI or there is at least 50% overlap between the ground truth and extracted ROI. The classifier trained on optimal set of features is tested using the remaining (unseen) regions as probe instances.

2.3 Results and Analysis

Images from the MIAS database [92] are used for evaluating the proposed saliency based framework for mass detection. The spatial resolution of images is $50\mu m \times 50\mu m$ and grayscale intensity quantized to

8 bits. The MIAS database is one of the most popular public databases used for evaluating breast cancer detection and diagnosis techniques. Though the database is old and many sophisticated algorithms have been applied to detect symptoms using this challenging database, the intricacy of the database is clearly visible from the results in the comparison study by Oliver *et al.* [71]. The database contains varied density mammograms for both mass and non-mass classes, which increases the intra-class variation and makes the problem even more challenging. There are total 322 MLO view mammograms in the database, both left and right breast images for 161 cases. Among the 322 mammograms, 207 are normal and 115 mammograms have one of the four symptoms of breast cancer. Further details about the number of images per symptom are summarized in Table 2.3.

Table 2.3: Symptom wise description of the MIAS database.

Description	**# Images (# Symptoms)**		
	Fatty	**Fatty-Glandular**	**Dense-Glandular**
Architectural Distortion	6(6)	6(6)	7(7)
Bilateral Asymmetry	4(4)	4(4)	7(7)
Mass	*24(27)*	*20(20)*	*12(12)*
Micro-calcification Cluster	6(6)	9(9)	10(15)
Normal	66	65	76
Total	**106**	**104**	**112**

In order to compare the performance of the proposed framework with existing algorithms, experiments are conducted with the experimental protocol used by Oliver *et al.* [71] and the performance is compared with seven state-of-the-art algorithms. The protocol includes classification of segmented regions as mass and non-mass using three times 10 fold cross-validation. The performance is compared in terms of mean and standard deviation values of Area Under the Curve (AUC) of Receiver Operating Characteristic (ROC) curves obtained after classification. Since we have used the same database and experimental protocol, performance of the proposed framework is directly compared with the results reported by Oliver *et al.* [71]. The performance of segmentation and classification steps of the proposed framework are individually discussed in the following sub-sections.

2.3.1 Segmentation Results

ROI segmentation using GBVS yields highly accurate results and does not generate any false alarm due to pectoral muscles on the MIAS database. 49 out of total 58 masses are detected by the saliency based segmentation, while nine are missed. Some false rejects are due to the noise in breast region, for example, as shown in Figure 2.10, when a label is coinciding with the breast tissues and therefore can not be completely removed. This results in false saliency accumulation at that point, resulting in missing the mass region as well as adding one false positive. The results from GBVS are promising and overall classification results (described in later subsections) justify the intuition to use saliency based segmentation for analyzing mammograms.

In this research, we also compare the performance of GBVS with three existing visual saliency algorithms - Esaliency [2], Hou and Zhang [51], and Liu *et al.* [63]. The algorithms are considered on the

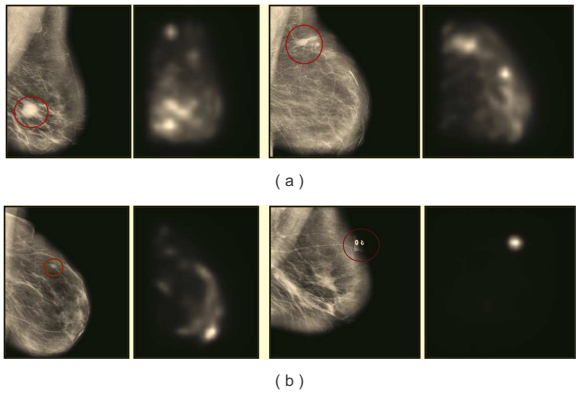

Figure 2.10: Sample results of the proposed saliency based segmentation algorithm. (a) Successful segmentation and (b) false segmentation.

basis of their capability to generate saliency map from an input grayscale image. Though the effectiveness of GBVS as a generic visual saliency algorithm can be analyzed in the benchmark study by Borji *et al.* [10], comparative analysis from Figure 2.11 and Table 2.4 show that GBVS outperforms other saliency algorithms for mammogram ROI segmentation. As shown in Table 2.4, three algorithms are able to detect more than half of the masses at the cost of high false positives. Additionally, unlike GBVS, other three algorithms are not able to distinguish between the pectoral muscle region and other breast parenchyma. The contrast of mass containing regions vary from other breast parenchyma, therefore, contrast maps being the basis of saliency map generation in GBVS makes it suitable for mammogram analysis.

Table 2.4: Comparative analysis of saliency algorithms.

Comparison Metric	**GBVS [44]**	**Liu *et al.* [63]**	**Hou & Zhang [51]**	**Esaliency [2]**
Mass detection ratio (threshold on saliency map)	$49/58$ (0.5)	58/58	$38/58$ (0.4)	$40/58$ (0.7)
False positives	$2-3$/image	NA	$6-7$/image	>10/image
Observation	Results are not affected by the presence of pectoral muscles	Entire breast region is the output salient object	Incorrect high saliency value in different regions of mammogram other than mass regions such as pectoral muscles and all corners of the image	It is not able to differentiate between the pectoral muscles and other breast parenchyma

2.3.2 Feature Extraction and Classification Results

In the proposed framework, $30,462$ overlapping circular regions are extracted from the probable regions marked by applying saliency based segmentation on 55 images containing 58 masses. $3,470$ regions contain at least 50% mass according to the ground truth data; these regions are considered as positive class (mass) samples. 154 features from seven different sets of features are computed to classify each

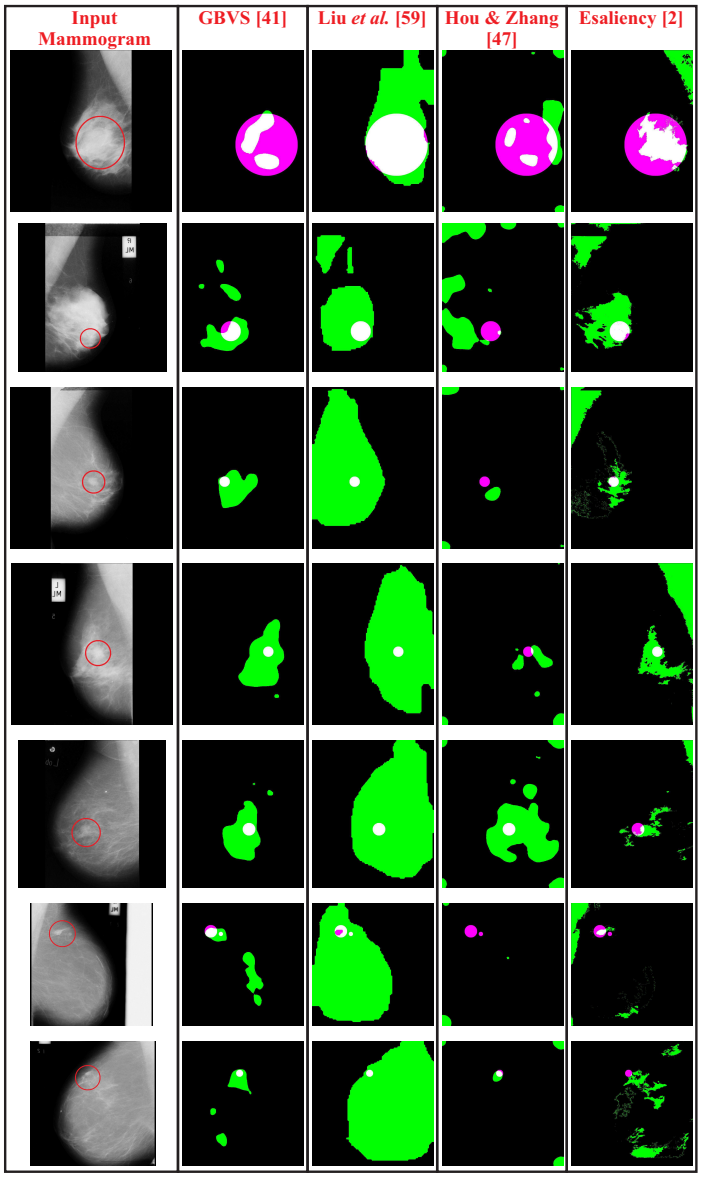

Figure 2.11: Sample results of the saliency algorithms. Each row corresponds to the output of the four saliency algorithms for corresponding mammogram image shown in the left most column. The green color in saliency maps denotes the ROI segmented after thresholding on the saliency map and pink color represents the ground truth region containing mass.

circular region as mass and non-mass. In the proposed framework, the performance of these features is evaluated thoroughly, starting from classification using individual sets of features. Feature selection techniques are applied on these feature sets to achieve optimal performance with minimum computational effort. The features with good classification performance are combined using feature concatenation to further enhance the classification performance. The results obtained from complete feature analysis are explained in this section.

Individual Feature Set Results

The performance of individual sets of features for *mass* vs *non-mass* classification of extracted regions can be compared in Table 2.5 and Figure 2.12. The results obtained can be summarized as follows,

Table 2.5: Classification results of individual sets of features.

Feature Category	**Features**	**No. of Features**	**AUC (A_z)**
Spatial Domain Features	GLRL Features	20	0.548 ± 0.016
	Intensity Features	5	0.532 ± 0.016
	Laws Texture Features	8	0.436 ± 0.059
	SGLD Features	65	0.687 ± 0.016
Fourier Domain Features	Spectral Energy Features	35	0.495 ± 0.015
Wavelet Features	DWT Entropy Features	9	0.876 ± 0.001
	RDWT Entropy Features	12	0.870 ± 0.001

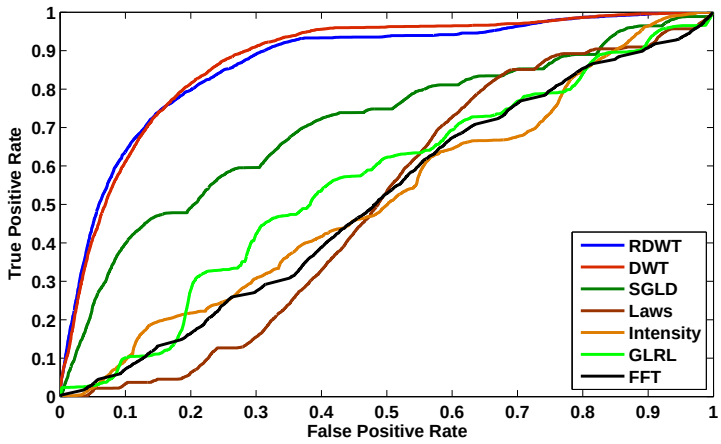

Figure 2.12: ROC curves for the individual sets of features (Best viewed in color).

- As compared to other feature sets, spatial domain features do not perform efficiently. One of the major reasons for the reduced performance could be varying orientation, shape and size of masses present in the circular ROIs. The results show that the intensity or texture information alone may not be sufficient to model the highly complex masses.
- Fourier domain spectral energies also could not yield high performance for the classifying circular regions. Since spatial information is absent in Fourier representation, spectral energies derived

from frequency bands alone may not be sufficient, therefore exploring additional features may be helpful for performance improvement.

- Entropy features from Discrete Wavelet Transform achieve show very good classification performance without being affected by the size or orientation of masses. Wavelet entropies model the randomness in edge maps along different orientations of a localized neighborhood. Therefore, they may be able to better encode the differences between mass and non-mass irrespective of their shape and size. Since the performance of DWT and RDWT features is dependent on the mother wavelet used, we have evaluated the results with 12 different mother wavelets. The results of this comparison are reported in Table 2.6. The results show that DWT entropy features derived from the first three levels of Bi-orthogonal 2.2 wavelet transform yields the best AUC of 0.876 ± 0.001.

Table 2.6: Comparing the performance of DWT and RDWT entropy features with different mother wavelets. The results are reported in terms of Area Under the Curve (A_z) of ROC curves.

Wavelet Used	**DWT**	**RDWT**	**DWT+RDWT**
Bi-orthogonal 1.3	0.863 ± 0.001	$\mathbf{0.870 \pm 0.001}$	0.874 ± 0.000
Bi-orthogonal 2.2	$\mathbf{0.876 \pm 0.001}$	0.848 ± 0.015	0.864 ± 0.000
Bi-orthogonal 5.5	0.821 ± 0.006	0.767 ± 0.044	0.863 ± 0.020
Coiflet 1	0.832 ± 0.020	0.792 ± 0.064	0.860 ± 0.000
Coiflet 5	0.812 ± 0.022	0.674 ± 0.044	0.847 ± 0.000
Daubechies 2	0.843 ± 0.012	0.784 ± 0.055	0.867 ± 0.001
Daubechies 10	0.788 ± 0.029	0.744 ± 0.052	0.874 ± 0.004
Discrete Meyer	0.775 ± 0.040	0.671 ± 0.064	0.842 ± 0.005
Reverse Bi-orthogonal 1.3	0.797 ± 0.009	0.618 ± 0.025	0.851 ± 0.000
Reverse Bi-orthogonal 2.2	0.855 ± 0.000	0.703 ± 0.051	$\mathbf{0.891 \pm 0.001}$
Reverse Bi-orthogonal 5.5	0.780 ± 0.058	0.786 ± 0.009	0.858 ± 0.008
Symlets 2	0.785 ± 0.036	0.721 ± 0.075	0.869 ± 0.001

- As discussed earlier, DWT can yield significant entropy features upto three levels of decimation and beyond that, the size of some decimated masses is insignificant for feature computation. Therefore, we have also evaluated the performance of Redundant Wavelet Transform features as there is no decimation step in RDWT. We empirically found that information upto level four is useful for the MIAS database. As shown in Table 2.6, the performance of RDWT entropy differs significantly from the corresponding DWT entropy features, which indicates that RDWT provides some additional information. Out of the 12 mother wavelets used for evaluation, entropy features derived from the RDWT representation using Bi-orthogonal 1.3 mother wavelet yields the best performance of $AUC = 0.870 \pm 0.001$.

Feature Selection Results

From the results reported in Table 2.5, it is clear that the performance of different feature sets differ significantly. Also, some features in these sets may be providing redundant information. Therefore, to reduce the computational effort and discard the redundant and irrelevant features in these individual fea-

ture sets, mRMR based feature selection [73] is applied to find the optimal features from these individual sets. The results obtained after feature selection are summarized in Table 2.7. It is observed that accuracy improved after feature selection for Spatial domain and Fourier domain features. Entropy features derived from DWT and RDWT depend on edge orientations within the region. However, due to varying shape and size of masses, their relevance can vary. Therefore, to keep the feature set generalizable, no further feature selection is applied on wavelet entropy features.

Table 2.7: Analyzing the effect of mRMR based feature selection on individual feature sets. Performance of individual set of features after mRMR based feature selection.

Feature Description	**No. of Selected Features**	**AUC (A_z)**
DWT	9	0.876 ± 0.001
RDWT	12	0.870 ± 0.001
Intensity	3	0.560 ± 0.047
FFT	21	0.523 ± 0.016
SGLD	52	0.719 ± 0.052
GLRL	15	0.631 ± 0.047
Laws	4	0.479 ± 0.093

Feature Combination Results

After thoroughly evaluating the individual sets of features, the feature sets are combined and classification performance is analyzed. Feature combination is performed at two levels - before feature selection and after feature selection, further described below.

- *Before feature selection:* As shown in Tables 2.5, the entropy values from DWT and RDWT representations yield best result among all features. Therefore, it is our assertion that any combination of features should contain these entropy features. Correlation analysis is also used to validate the combination. The class-wise correlation between the distance scores obtained after SVM classification is calculated for both the feature sets. The correlation for the positive class (mass) is found to be 0.33, which indicates that True Positive (TP) to False Positive (FP) ratio on the ROC curve can be improved when DWT and RDWT features are combined. DWT features from all 12 mother wavelets are combined with their corresponding RDWT features. Comparison results from Table 2.6 and Figure 2.13 show that the features extracted using Reverse Bi-orthogonal 2.2 mother wavelet yields the best TP-FP ratio with $AUC = 0.891 \pm 0.001$. The combination of best performing DWT and RDWT features from Bi-orthogonal 2.2 and 1.3 mother wavelets respectively could not perform better than DWT and RDWT features derived from Reverse Bi-orthogonal 2.2 mother wavelet.

- *After feature selection:* The feature sets obtained after feature selection are concatenated with combination of DWT and RDWT to analyze the scope for further improvement in the classification performance. Feature combination results are summarized in Table 2.8 and Figure 2.14. Along with evaluating individual features, feature set obtained by combining the individual sets

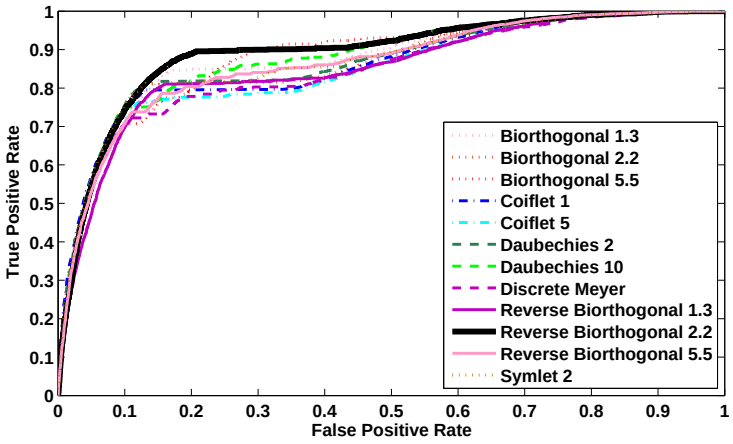

Figure 2.13: ROC curves for different mother wavelets with combined features from DWT and RDWT (Best viewed in color).

of features is also analyzed using mRMR based feature selection and PCA based dimensionality reduction. The combined feature set consists of DWT, RDWT, SGLD, GLRL, and FFT features (intensity and Laws features are discarded for the combination due to their poor performance). The results derived from feature combination, as reported in Table 2.8, show that the highest classification performance is achieved using the combination of DWT and RDWT features only.

Table 2.8: Analyzing classification performance with different combinations of feature sets.

Feature Description	**No. of Features**	**AUC** (A_z)
DWT + RDWT	21	$\mathbf{0.891 \pm 0.001}$
DWT + RDWT + Intensity	24	0.754 ± 0.039
DWT + RDWT + GLRL	36	0.747 ± 0.025
DWT + RDWT + FFT	42	0.489 ± 0.042
DWT + RDWT + SGLD	73	0.693 ± 0.020
DWT + RDWT + FFT + GLRL + SGLD (Complete Feature Set)	141	0.457 ± 0.073
mRMR based Feature Selection (On Complete Feature Set)	114	0.788 ± 0.030
PCA based Dimensionality Reduction (On Complete Feature Set)	10	0.463 ± 0.033

Comparison with Existing Algorithms

The proposed framework uses saliency based region of interest detection. The segmented regions are further refined using SVM based classification with entropy features derived from DWT and RDWT representations. The performance of the proposed framework can be directly compared with the results reported by Oliver *et al.* [71] as the experimental protocol and database are same. Therefore, the comparison is performed with seven state-of-the-art algorithms evaluated in [71] that use computer vision

algorithms such as Difference of Gaussian (DoG) and isocontour maps for segmentation of regions of interest, followed by machine learning approach for false positive reduction. The algorithms are analyzed in the literature review section in Table 2.1 and the results are shown in Table 2.9. The results in Table 2.9 clearly shows that the proposed algorithm achieves significant improvement in reducing false positives while detecting masses in digital mammograms with improved sensitivity.

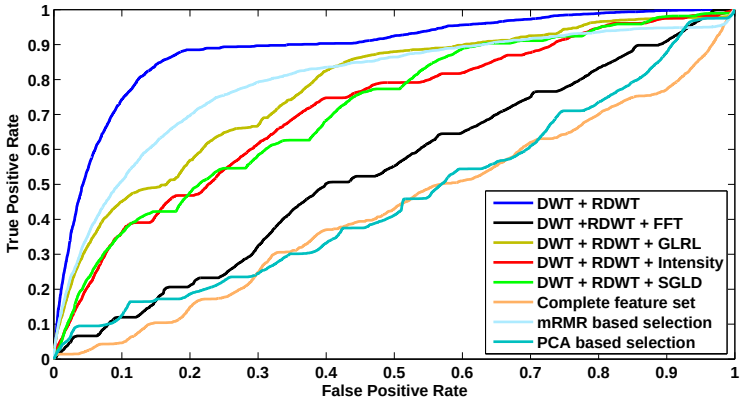

Figure 2.14: ROC curves for different combinations of feature sets (Best viewed in color).

Table 2.9: Comparing the performance of proposed algorithm with existing algorithms on the MIAS database.

Algorithm	**AUC** (A_z)
Detection using Difference of Gaussian [77]	0.601 ± 0.028
Detection using concentric layers of gray regions [28]	0.614 ± 0.032
Detection based on a classifier [53]	0.673 ± 0.016
Pattern matching based approach [58]	0.675 ± 0.005
Thresholding based approach [54]	0.685 ± 0.002
Laplacian edge detector based approach [75]	0.758 ± 0.005
Detection using Iris filter [97]	0.787 ± 0.003
Proposed framework with DWT and RDWT features	$\mathbf{0.891 \pm 0.001}$

2.4 Summary

This chapter presented a novel framework to detect mass(es) from screening mammograms for diagnosis of breast cancer. The detection of mass(es) from screening mammograms has been a challenging problem due to inherent complexity of size, shape, and surrounding tissue structures. Several techniques have been proposed and comparative studies have been conducted to evaluate the state-of-art techniques on public datasets. The proposed framework utilize the saliency based algorithm to detect mass containing regions which does not require any segmentation of pectoral muscles unlike most of the existing techniques. The experimental analysis conducted on public database using existing protocol concludes that proposed framework outperforms state-of-the-art techniques.

Chapter 3

HEp-2 cell image classification using Laws texture features

3.1 Introduction

Human immune system consists of cells and tissues which work together to defend the body from foreign infections. The immune system is composed of two components, innate immune system and acquired immune system. The innate immune system is responsible for activation of white blood cells to protect the body against foreign infections without using any antibodies (which are developed as part of the adaptive or acquired immune system as the human grows). Acquired immune system learns to fight infections and preserve the learning for possible future infections. It activates immune cells and generate proteins i.e., antibodies according to the learned patterns in order to protect against foreign invasions. When the acquired immune system mistakenly learns to fight against self-tissues, the antibodies thus generated are called autoantibodies. This phenomenon is referred as autoimmunity and the resulting syndromes are known as autoimmune diseases. The reasons for such a malfunctioning in the acquired immune system are unclear; however, they are considered to be the combined effect of genetic, environmental, and regulatory changes [84]. For instance, a patient with genetic conditions favorable to development of autoimmunity, under specific environmental conditions, may become a victim of a foreign intrusion which might result in triggering a particular disease. The effects of autoimmune disease vary according to the targeted part of the body which can be heart, brain, glands, digestive system, or blood vessels. Some autoimmune diseases such as Systemic Lupus Erythematosus (SLE) and Type 1 diabetes can even affect multiple parts of the body including essential organs such as kidneys, muscles, and blood vessels. Collectively, autoimmune diseases are one of the leading causes of deaths worldwide. Satoh *et al.* [85] have shown that in USA alone, autoantibodies are present in more than 32 million individuals. Further, Fairweather *et al.* [29] suggest that the autoimmune diseases are more prevalent among women and their overall prevalence is increasing. Mostly autoimmune diseases are chronic syndromes with debilitating health issues and a never ending clinical treatment; however, some of them may even lead to death.

3.1.1 Diagnostic tests for Autoimmune Diseases

The most common symptom of autoimmunity is inflammation which leads to reddish scars, pain, and swelling. While the cure for autoimmune diseases is under exploratory phases, currently treatments are conducted to reduce the symptoms and effects associated with the particular disease. In current treatment process, it is important to detect and diagnose autoimmune diseases, for which the following tests are useful [17]:

- **Laboratory Evaluation:** Autoimmune diseases resulted due to inflammation cause significant changes in the normal hematology. Therefore, laboratory evaluations such as Complete Blood Count (CBC) and urinalysis are conducted to investigate any abnormality in hematologic parameters such as white blood cell count and red blood cell count.
- **Inflammatory Markers:** In order to confirm commonly observed abnormalities in autoimmune diseases, tests indicative of inflammation are conducted. Some of the popular tests include Erythrocyte Sedimentation Rate (ESR) and C-Reactive Protein (CRP).
- **Autoantibody Tests:** The presence of autoantibodies combined with appropriate symptoms helps to support diagnosis for autoimmune diseases. Autoantibodies are of various types, therefore, different tests are conducted to investigate the presence of particular autoantibodies. However, among various types, the presence of Antinuclear Antibodies (ANA) has been commonly observed for many autoimmune diseases. Therefore, Antinuclear Antibody Test is conducted as a screening test for autoimmune diseases.

Among all the diagnostic tests, detecting the presence of autoantibodies is vital for diagnosis of autoimmune diseases. However, ANA testing is a time consuming and expensive process due to the involvement of human experts and lack of automated techniques [21] [26]. Significant efforts are being made to develop automated systems which could fasten the diagnostic process.

3.1.2 ANA Testing

ANA tests are conducted to detect the presence of antinuclear antibodies which help in diagnosis of several autoimmune diseases. Enzyme-Linked Immunosorbent Assay (ELISA) and Indirect Immunofluorescence (IIF) are the two widely used methods for detection of anitnuclear antibodies. Even though both ELISA and IIF achieve high sensitivity, IIF is preferred and the recommended procedure [66]. IIF achieves high sensitivity as well as specificity for ANA detection and can be used to detect many antinuclear antigen patterns unlike ELISA which is a targeted test to detect specific patterns [36]. Similar to several other medical diagnostic tests, the clinical procedure of IIF is time consuming and requires human experts for visualization. Firstly, experts categorize the digitally captured images of IIF slides based on the fluorescence intensity levels in the images. The images categorized as appropriate for clinical diagnosis are then further examined to identify the antigen patterns being exhibited as a result of antigen reactions taking place within Human Epithelial Type 2 (HEp-2) cells. The increasing number of tests being conducted resulted in need for automated systems in place of manual examination of test slides.

To the best of our knowledge, the IIF procedure has been automated up to the generation of test slides with the help of robotics and vision based techniques [83]. Very few commercial systems have automated the steps in manual examination of IIF images [5]. However, a completely automated computer aided diagnostic (CAD) system for this test is still not available. The automation of pattern identification from test slides would not only reduce the need for large number of human experts, it would also help in standardization of the test. Such a standardization would establish confidence among the test results by omitting the possibility of intra-observer variability.

3.1.3 Research Contribution

As mentioned previously, the state-of-art procedure for ANA testing is IIF test which reports the presence of antinuclear antibodies within the patient's serum. Though IIF is very useful as clinical screening for autoimmunity, this procedure lacks standardized completely automated processing and requires human experts to examine the fluorescence microscopic images. Therefore, significant efforts are underway to develop efficient techniques to automate this procedure [7], [82]. Most challenging task in automating the IIF procedure is identification of patterns from HEp-2 cells within the test images. Recently, public databases are made available that have significantly driven the research efforts in automating the task of pattern identification [32]. Many sophisticated pattern classification approach based techniques have been developed and high performance results are reported on common protocols. In this study:

- We review the existing literature and critically analyze the shortcomings observed by most of the researchers. Using innate characteristics of a cell image, we propose to categorize the features used by existing techniques and some other related features that could also be used for classification.
- We propose to use Laws texture features [59] for HEp-2 cell image classification and present comparative results with other features using different classification algorithms. Also, results are computed on different databases to analyze the impact of data from different labs on the classification performance.
- We analyze the classification performance of different feature sets on multiple classification algorithms using public databases on existing and a k-fold cross validation based protocols.

3.2 Pattern identification from IIF slides

The IIF test slide images are generated by capturing fluorescent radiation exhibited as a result of antigen reaction within the HEp-2 cells. The exhibited patterns help in identification of different types of antigens present in the serum thereby leading to detection of rheumatic diseases. Since the fluorescence radiation is vulnerable to ambient light, the image of IIF test slide is generally categorized as positive, intermediate, and negative fluorescence image [83]. The categorization is based on the quality of captured image thereby indicating the usability of image for diagnosis. Positive images are high quality fluorescence images as they are high contrast images enabling the expert observers to easily identify the patterns

being exhibited. The images labelled with intermediate fluorescence are lower in contrast, therefore, it is relatively difficult to identify antigen patterns from intermediate images as compared to positive images. Finally, negative fluorescence images do not qualify for any further clinical usage. The positive and intermediate images are examined to identify antigen patterns. Identification of patterns from the fluorescent HEp-2 cell images can be viewed as a classical pattern recognition problem with more than 50 possible target classes. This section emphasizes on the efforts being made to automate the process of pattern identification from IIF test slides. As illustrated in Figure 3.1, an automated system for analysis of IIF images comprises of the following steps:

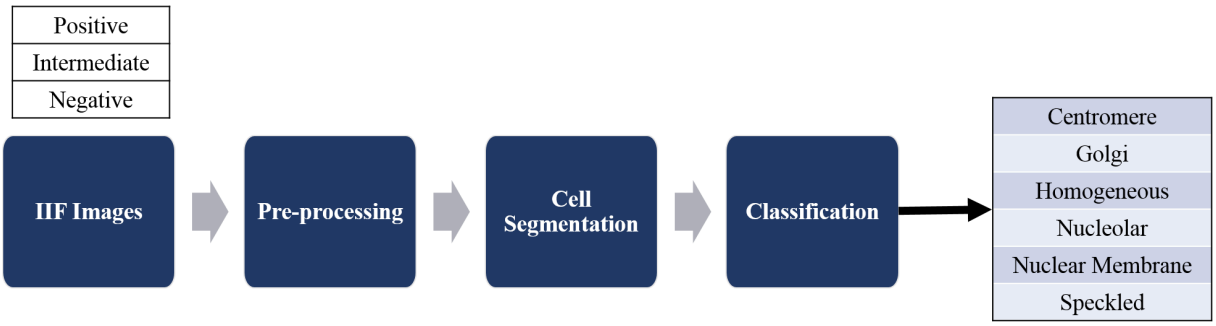

Figure 3.1: Steps involved in an automated system for diagnosis of IIF images.

- **IIF Image Classification:** Digitally captured IIF image is first labeled as positive, intermediate or negative intensity image based on the quality of fluorescent radiation as perceived from the digital image. Only positive and intermediate intensity images are considered for further analysis. Figure 3.2 illustrates samples of positive and intermediate intensity IIF images.

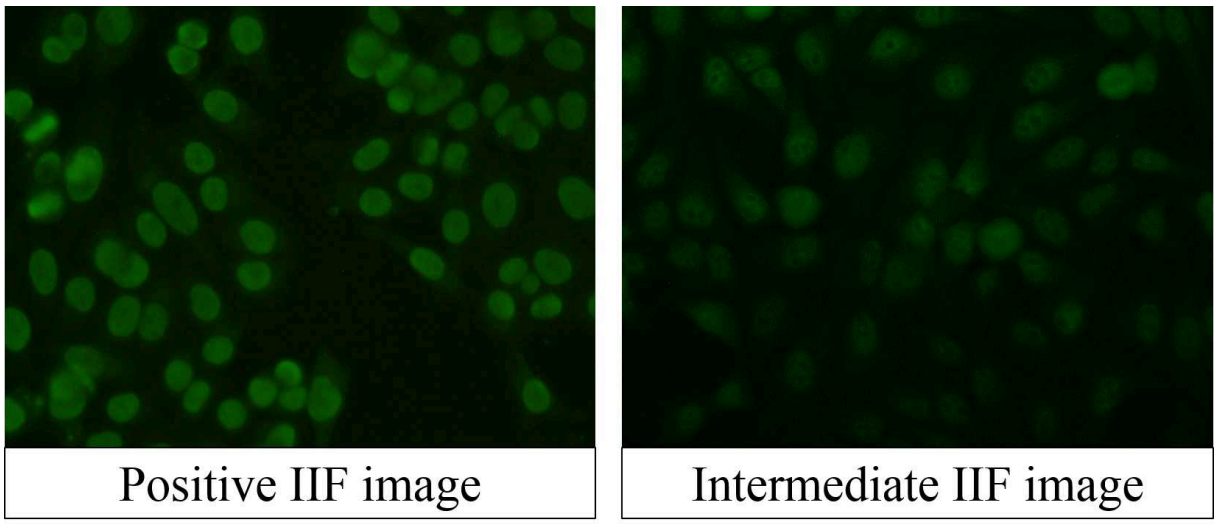

Figure 3.2: A sample of positive and intermediate intensity IIF images.

- **Pre-processing:** IIF images are colored images, however, Cordelli and Soda [22] suggest that converting color images to grayscale representation improves the efficiency of automated process. Moreover, mechanically captured images may incur some calibration errors resulting in out of

focus images, therefore, some pre-processing steps may also be required to correct such errors. Collectively a pre-processing step is essential before further analysis is performed on IIF images.

- **Cell Segmentation:** Image segmentation techniques are required to segment the HEp-2 cells from the IIF image. An example is shown in Figure 3.3. As discussed earlier, positive intensity IIF images are higher in contrast as compared to intermediate images; therefore, any segmentation algorithm for IIF images need to be designed carefully. A common segmentation algorithm may result in less accurate results for both types of images. Mostly existing techniques have utilized Otsu thresholding [72] for cell segmentation [52], [27], [46]; however, most of these techniques fail when cell structures are not segmented accurately [23]. Significant efforts are required to develop efficient techniques for HEp-2 cell segmentation from IIF images.

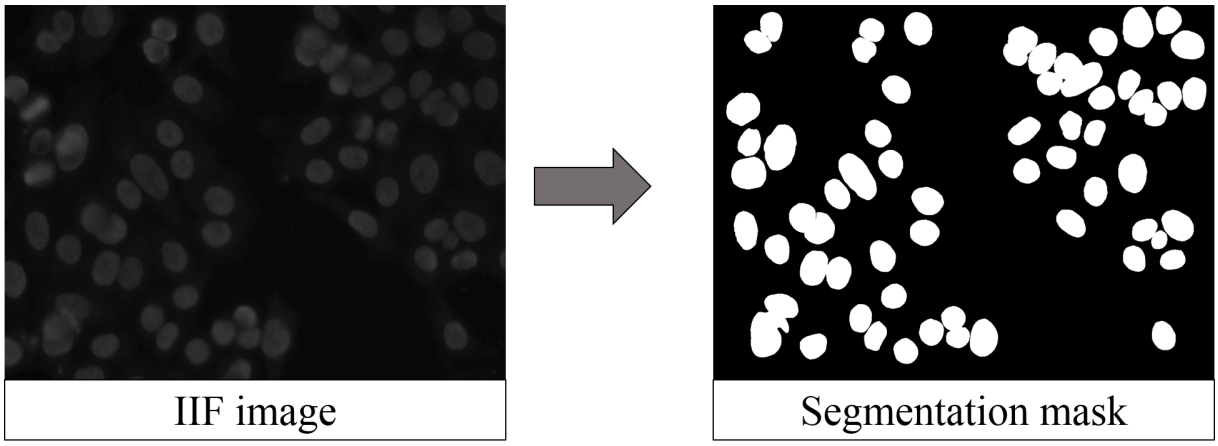

Figure 3.3: Segmentation mask for corresponding IIF image.

- **HEp-2 Cell Image Classification:** The segmented HEp-2 cell images are then classified among target antigen patterns using pattern recognition and machine learning techniques. The public datasets have focused on commonly observed antinuclear antigen patterns such as Centromere, Golgi, Homogeneous, Nucleolar, Nuclear Membrane, and Speckled. Figure 3.4 illustrates a sample of these antigen patterns in both positive and intermediate intensity IIF images. Similar to the segmentation step, classification techniques need to consider the difference in properties between intermediate and positive intensity images.

3.3 HEp-2 Cell Image Classification

Efforts are being made to promote research and development of techniques to automate HEp-2 cell image classification. Public databases are being released through workshops and competitions in reputed international conferences such as International Conference on Pattern Recognition (ICPR) [32] [49] and International Conference on Image Processing (ICIP) [48]. Availability of such public databases have largely driven the research for HEp-2 cell image classification. The initial approaches submitted during

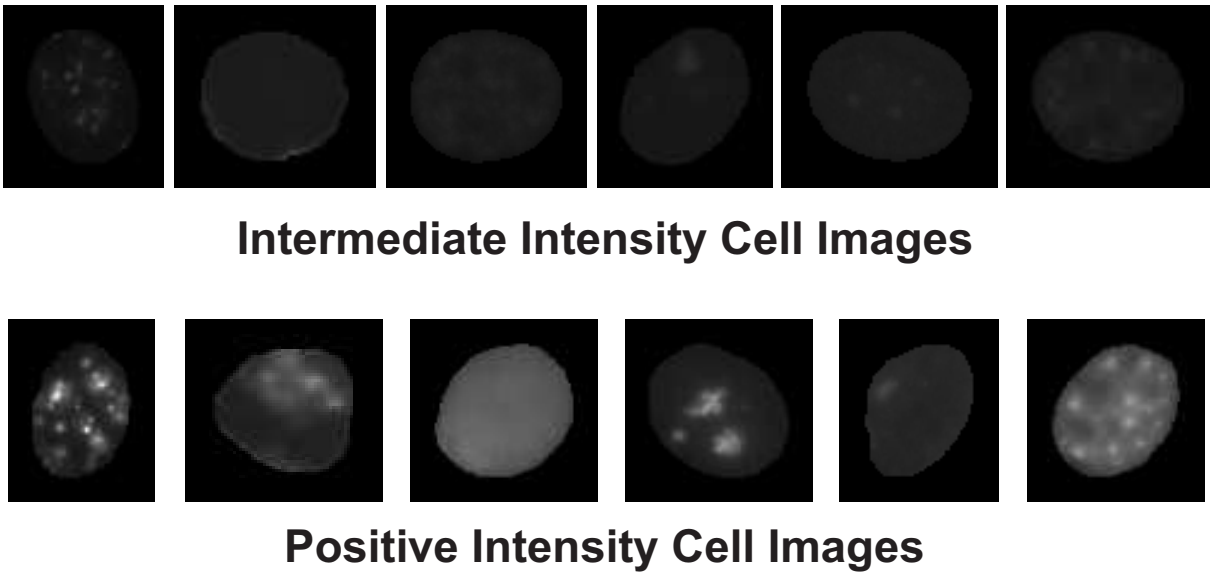

Figure 3.4: Sample images from the ICIP 2013 cell image classification contest training dataset [48]. The cell pattern types of images from left to right - Centromere, Golgi, Homogeneous, Nucleolar, Nuclear Membrane, and Speckled.

the ICPR 2012 contest on HEp-2 cell image classification have evaluated various image based features in order to find the optimal set of features [32].

In this research, we categorize the features used by most of the existing approaches based on various object based properties of a HEp-2 cell image. Under the purview of proposed feature categorization, we present a review of existing literature and discuss the research gaps observed in research associated with HEp-2 cell image classification. We propose the use of Laws texture features for HEp-2 cell image classification task validated by comparative experiments. Also, we analyze the results reported by existing techniques and the protocols with supportive experimental analysis.

3.3.1 Literature Review

In the initial study conducted by Foggia et al. [32], many researchers used geometric features along with other intensity based features for HEp-2 cell image classification. As summarized in Table 3.1, recent techniques have largely explored only intensity based features; specifically descriptor features. The results from a comparison study by Snell et al. [89] report high performance using shape based features. However, most of the techniques incorporate texture or descriptor based features in combination with standard classification algorithms, such as Support Vector Machines (SVM) [96] and k-Nearest Neighbour (kNN) [35], to develop efficient models for HEp-2 cell image classification. In this study, existing literature is summarized with respect to a proposed feature categorization. We broadly categorize different features used by existing techniques for HEp-2 cell image classification in four categories.

Table 3.1: Review of existing literature based on the proposed feature categorization and classification techniques used for HEp-2 cell image classification.

Reference	Features				Technique	Database
	Geometric	Texture	Descriptor	Others		
Perner et al. [74]	Y				Decision tree	Private data
Soda and Iannello [90]		Y			Aggregation of binary classifiers	Private data
DiCataldo et al. [18]	Y	Y	Y		Subclass Discriminant Analysis	MIVIA
Faraki et al. [30]				Y	Bag of words	MIVIA
Kong et al. [55]			Y		Sparse coding	MIVIA
Liu and Wang [62]				Y	Support Vector Machine	MIVIA
Nanni et al. [68]			Y		Support Vector Machine	MIVIA
Nosaka and Fukui [69]			Y		Support Vector Machine	MIVIA
Ponomarev et al. [78]	Y				Support Vector Machine	MIVIA
Shen et al. [87]			Y		Bag of words	MIVIA
Snell et al. [89]	Y	Y	Y		Support Vector Machine	MIVIA
Stoklasa et al. [91]	Y	Y	Y		kNN based classifier	MIVIA
Theodorakopoulos et al. [95]			Y		Sparse representation	MIVIA
Wiliem et al. [101]			Y		Bag of words	MIVIA
Yang et al. [102]				Y	Support Vector Machine	MIVIA

Feature Categorization

The proposed feature categorization is based on the properties of a HEp-2 cell image which could be captured as features and may be helpful in antigen pattern classification:

1. **Geometric Features:** Features that focus on various geometric aspects and relate to the characteristics associated with shape, size, and circumference of HEp-2 cells are referred as geometric features.

2. **Texture Features:** Features which directly relate to the texture or intensity pattern of a cell image are generally defined as texture features. The feature representations in this category are Laws texture features [59], Spatial gray level dependence features (SGLD) [43], and Gray level run length features (GLRL) [94].

3. **Descriptor Features:** Descriptor features correspond to the feature computations which involve specific keypoint based description or generate histogram based descriptors from feature maps. Some examples are Local Binary Pattern (LBP) [70], Scale Invariant Feature Transform (SIFT) [64], and Histogram of Oriented Gradients (HOG) [24].

4. **Others:** This category includes feature representations such as statistical features computed from the intensity values in a cell image [41], features based on dictionary learning [30], and features derived based on ICA or PCA projections [62], [102].

Literature Analysis

According to the proposed categorization, existing literature is summarized below:

- **Geometric Features:** Ponomarev et al. [78] utilize the shape and structure based features for SVM based classification. Perner et al. [74] developed a data mining based decision tree to classify the HEp-2 cell images using the shape and size based features.

- **Texture Features:** DiCataldo et al. [18] proposed a Subclass Discriminant Analysis based approach which uses a combination of texture and shape based features. Stoklasa et al. [91] combined multiple shape and texture features to propose an efficient kNN based technique. Soda and Iannello [90] proposed an aggregation of classifiers based technique which incorporates various texture features.

- **Descriptor Features:** Nanni et al. [68] proposed an ensemble of variants of LBP features in combination with SVM based classification. Nosaka and Fukui [69] explored a rotation invariant co-occurrence among adjacent LBPs in combination with SVM based classification. Other than standard classification models, researchers have also utilized learning based models. Kong et al. [55] combined LBP and HOG features to develop a dictionary learning based approach. Theodorakopoulos et al. [95] utilized SIFT and LBP to develop a sparse representation based technique. Wiliem et al. [101] proposed an advanced learning approach based on bag of visual

words which incorporates SIFT based features. Shen et al. [87] proposed a framework which uses intensity order pooling based rotation invariant local gradient features for a bag of words based classification.

- **Others:** Researchers have also tried to learn discriminating features from cell images to develop task specific classification models. Liu and Wang [62] learned discriminating features from images in a learning based approach. Yang et al. [102] proposed to learn features using Independent Component Analysis based framework for a SVM based multi-class classification. Faraki et al. [30] adopted a dictionary learning approach to develop fisher tensors based technique.

Significant efforts are also being made by the biomedical industry to develop efficient CAD techniques for IIF testing. Bizarro et al. [5] analyzed and compared the performance of six commercial systems being used by clinicians for IIF testing. Their analysis was mainly aimed at comparing the classification performance of six systems for positive vs negative fluorescence categorization of IIF images. The results show that commercial systems yield good performance for positive vs negative classification task. Though, they have also reported results for the HEp-2 cell image classification; however, the commercial systems do not show high performance.

3.3.2 Databases and Existing Results

HEp-2 cell image classification research has surged since the release of MIVIA dataset during ICPR 2012 [32]. The MIVIA dataset comprises of about 1400 cell images pertaining to six cell categories. Another bigger database has been released as training set during ICIP 2013 cell classification competition [48]. Table 3.2 provides summary of MIVIA and ICIP 2013 datasets. As shown in Table 3.1, the existing techniques are generally evaluated using the two predefined protocols on MIVIA dataset.

- *Protocol 1* - An equal split of total cell images into single training and testing datasets as provided during the ICPR 2012 HEp-2 cell image classification contest.
- *Protocol 2* - Leave-one-out cross validation on entire dataset i.e, during each fold of 28 fold cross validation, 27 images are to be used for training and the left out image is used to test the performance of trained classifier.

The results from existing literature on the two protocols using MIVIA dataset are summarized in Tables 3.3 and 3.4. The results reflect following key insights:

- The results from existing literature are encouraging and show the HEp-2 cell image classification is a complex pattern recognition problem with maximum overall accuracy of 75.10% and 89.55% on protocol 1 and protocol 2, respectively. However, significant efforts are required to attain clinically usable accuracy value close to 100%.
- The results summarized in Table 3.4 depict that coarse and fine speckled are the most difficult to identify among the six antigen patterns and the highest accuracies are observed for homogeneous and centromere patterns.

- The image wise results show a huge variation in correct classification rate across the 28 images. Most of the positive intensity images are classified correctly, whereas, the accuracy for intermediate intensity images is significantly low.
- Even for positive intensity category, poor performance is observed in few cases. The variations in accuracy may be attributed to the complexity of combined model for positive and intermediate intensity images.

Table 3.2: Summary of the MIVIA dataset [32] and training dataset provided during ICIP 2013 cell image classification contest [48].

Database	Pattern	Positive	Intermediate	Total
MIVIA	Centromere	173	184	357
	Coarse Speckled	136	74	210
	Cytoplasmic	36	75	111
	Fine Speckled	97	111	208
	Homogeneous	222	108	330
	Nucleolar	129	112	241
	Total	793	664	1457
ICIP 2013	Centromere	1378	1363	2741
	Golgi	349	375	724
	Homogeneous	1087	1407	2494
	Nucleolar	934	1664	2598
	Nuclear Membrane	943	1265	2208
	Speckled	1457	1374	2831
	Total	6148	7448	13596

Table 3.3: Overall cell classification accuracy (%) reported in existing literature on MIVIA dataset.

Citation	Protocol 1	Protocol 2
DiCataldo et al. [18]	72.21	89.55
Faraki et al. [30]	70.16	71.70
Kong et al. [55]	66.76	63.16
Liu and Wang [62]	66.60	58.92
Nanni et al. [68]	70.00	67.20
Nosaka and Fukui [69]	68.53	70.65
Ponomarev et al. [78]	70.57	54.77
Shen et al. [87]	74.39	69.39
Snell et al. [89]	56.50	53.70
Stoklasa et al. [91]	64.40	64.30
Theodorakopoulos et al. [95]	75.10	64.90
Wiliem et al. [101]	67.40	56.80
Yang et al. [102]	64.60	60.60

Table 3.4: This table presents the number of correctly classified cell images for each IIF image as reported by existing techniques using leave-one out cross validation protocol on MIVIA dataset.

Sr.	Pattern	Catg.	#Img	[18]	[30]	[55]	[62]	[68]	[69]	[78]	[87]	[91]	[95]	[101]
1	Homogeneous	P	61	61	57	61	60	54	59	49	60	61	54	43
2	Fine Speckled	I	48	42	25	48	29	14	17	16	18	33	32	19
3	Centromere	P	89	89	89	89	88	79	88	86	87	83	88	87
4	Nucleolar	I	66	57	21	12	29	17	31	27	44	3	26	32
5	Homogeneous	I	47	46	16	47	35	35	42	27	30	43	28	26
6	Coarse Speckled	P	68	65	66	68	10	26	63	63	29	63	36	44
7	Centromere	I	56	49	47	56	49	22	37	47	54	34	51	54
8	Nucleolar	P	56	55	17	56	0	51	30	11	25	43	5	30
9	Fine Speckled	P	46	40	6	46	15	7	23	6	14	34	4	23
10	Coarse Speckled	I	33	29	22	26	5	32	11	12	33	14	23	16
11	Coarse Speckled	I	41	39	30	41	34	35	30	5	41	13	34	32
12	Coarse Speckled	P	49	49	36	38	35	33	37	37	43	43	41	35
13	Centromere	P	46	46	42	34	34	44	44	38	35	40	42	30
14	Centromere	I	63	14	40	63	4	45	25	5	8	0	3	30
15	Fine Speckled	I	63	39	17	33	21	11	23	14	24	16	46	36
16	Centromere	P	38	37	36	35	35	38	36	35	33	38	38	36
17	Coarse Speckled	P	19	14	5	2	0	3	0	9	4	2	2	14
18	Homogeneous	P	42	41	42	42	26	23	32	7	27	17	18	14
19	Centromere	I	65	63	57	57	64	62	61	48	62	48	52	56
20	Nucleolar	I	46	45	44	46	7	42	38	6	43	30	2	41
21	Homogeneous	I	61	44	22	3	23	37	25	45	20	21	17	50
22	Homogeneous	P	119	115	104	86	102	84	83	65	81	78	92	78
23	Fine Speckled	P	51	49	41	48	35	18	31	1	14	34	16	28
24	Nucleolar	P	73	69	66	65	66	68	65	56	68	55	63	45
25	Cytoplasmic	I	24	22	13	24	4	19	20	11	18	9	19	10
26	Cytoplasmic	P	36	34	33	34	33	33	32	30	34	32	34	33
27	Cytoplasmic	I	38	37	36	38	35	34	32	31	37	35	37	35
28	Cytoplasmic	I	13	13	13	13	13	13	13	10	13	13	12	10

3.4 Proposed Laws Texture Features Based HEp-2 Cell Image Classification

Above literature analysis depicts that intensity based features are generally more efficient for HEp-2 cell image classification. However, most discriminating features are still unclear and yet to be established. Other than several texture features, such as SGLD features [43] and GLRL features [94], being used for computer vision applications, Laws texture features [59] have been used effectively for specific medical image analysis applications such as mammography [77]. Laws texture features are derived from basic linear kernels that represent edges, ripples, waves, lines, and spots in a square region. Based on the insights from patterns within the HEp-2 cell images [48], we propose to use Laws texture features for the HEp-2 cell image classification, as shown in Figure 3.5. We perform experimental analysis to evaluate and compare the performance of Laws texture features in the proposed system with other widely used image based features for HEp-2 cell image classification such as LBP and HOG features.

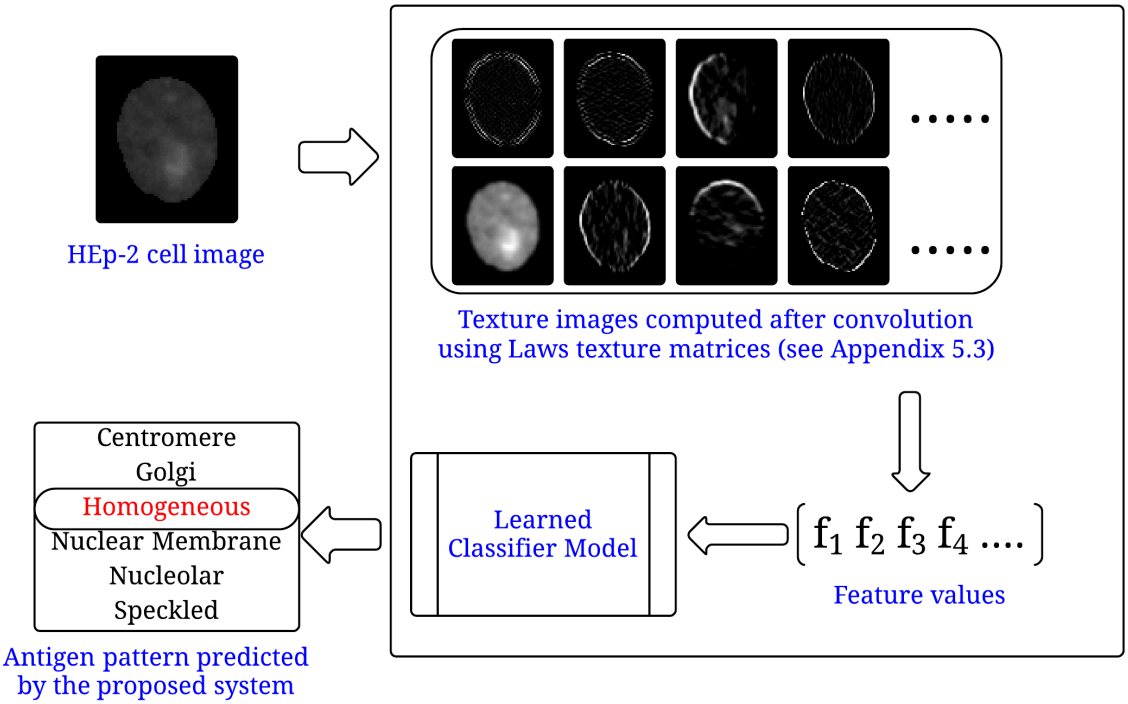

Figure 3.5: Diagrammatic representation of proposed Laws texture features based HEp-2 cell image classification.

3.4.1 Algorithm

The input to the proposed system, as illustrated in Figure 3.5, is the HEp-2 cell image segmented from IIF test slide image. In order to identify the antigen pattern in input image, Laws texture features are extracted. Laws texture features consist of total 102 statistical values computed from the 34 feature maps (illustrated in Figure 3.5) obtained from the convolution of feature masks with the HEp-2 cell image, see

Appendix 5.3 for more details. These features are then served to a trained classifier model for pattern identification. The classifier model is developed using the features computed from the training samples. Rest of this section evaluates the effectiveness of the proposed Laws texture features based system and compares the performance with other widely used feature representations.

3.4.2 Experimental Database and Protocol

In order to evaluate the effectiveness of Laws texture features, we perform several comparison experiments. Various features are tested using four different classifiers to ensure optimal performance. The results are obtained using two public datasets - MIVIA [32] and the training dataset provided during ICIP 2013 [48]. Thus, the aim of entire analysis are:

- to compare and evaluate the performance of Laws texture features for the HEp-2 cell image classification,
- to validate the comparative results using images from two different datasets, and
- to validate our assertion that instead of using a single classifier model with same parameter values for both positive and intermediate intensity images, different classifier models need to be developed for better classification.

Features and Classifiers

In order to compare the performance of Laws texture features, we have considered features from spatial, frequency as well as wavelet domain representations of cell images. Wavelet transforms are used to represent the frequency domain so that the spatial information also remain intact while computing important frequency domain characteristics. The entire pool of features according to above mentioned categorization is summarized below:

- **Geometric Features:** Geometric features include shape, size, and boundary based features such as area, convex hull features, solidity, aspect ratio, compactness, and Fast Fourier Transform based spectral energy features computed via boundary points [11].
- **Texture Features:** Gray Level Run Length features (GLRL) [94], Laws texture features [59], Energy and entropy values computed from high frequency bands of Redundant Discrete Wavelet Transform representation [34], Gabor wavelet features, and Spatial Gray Level Dependence features (SGLD) [43] are considered for texture based features.
- **Descriptor Features:** Descriptors computed from HOG [24] and uniform circular LBP [70] representations are considered for descriptor features.
- **Others:** Statistical features computed from intensity distribution of HEp-2 cell images, such as mean, absolute mean, and standard deviation are also used for comparison.

Classification algorithms considered for the analysis are: k-Nearest Neighbor [35], Random Decision Forests [47], SVM [96] with linear kernel, and SVM with non-linear RBF kernel. Parameter selection for SVM is performed using grid search [19] to ensure best results.

Experimental Protocol

The experiments are conducted to evaluate our assertion that separate models should be developed for positive and intermediate intensity images. Therefore, we divided both datasets into respective positive and intermediate intensity datasets. Along with the positive and intermediate models, another model is developed using the entire data, i.e. combined positive and intermediate intensity images, to analyze its impact on performance. All the three models are evaluated using existing protocols of MIVIA dataset (discussed in Section 3.3.2; 50-50 split protocol 1 and leave one out protocol 2) as well as 10 fold cross-validation protocol (i.e. 10 equal size folds for each class are created, nine folds are used for training and one fold is used for testing. This training and testing is repeated 10 times and average accuracy is reported).

3.4.3 Results and Analysis

Table 3.5 summarizes the comparison of classification results of different feature and classifier combinations using the two protocols of MIVIA and the 10 fold cross validation protocol on MIVIA dataset. The high accuracy values using 10 fold cross validation protocol clearly indicate the limitation in existing protocols of MIVIA dataset. Also, the cross-validation based experimental protocol convey similar results irrespective of the dataset, see Figure 3.6. The overall analysis from Figure 3.6 can be summarized as:

- Laws texture features are effective for HEp-2 cell image classification. They perform the best on ICIP 2013 contest training dataset as well as show high accuracy similar to LBP and HOG features for MIVIA dataset. The results on two different datasets also signify the robustness of these features across data from multiple sources.
- Texture and descriptor features outperform all other feature categories for the positive intensity and intermediate intensity sets. As discussed earlier, though the images pertaining to intermediate intensity set are difficult to categorize, intensity based features yield significant improvement in classifying these images.
- The results further indicate that cells across different types of cell patterns have similar shape and size thereby increasing the inter-class similarity. On the other hand, grayscale distribution within different cell classes vary significantly thus increasing the inter-class variability. Therefore, the features based on grayscale values such as texture and descriptor features yield better performance for cell image classification than geometric features.
- Among the four classification techniques used for experiments, SVM with RBF kernel yields the highest accuracy for HEp-2 cell image classification. The results of RDF and SVM-RBF are

comparable with RDF providing the second best classification accuracy.

- The intermediate intensity images are generally lower in contrast as compared to positive intensity images. The results in Figure 3.6 present a comparison of the three models trained on positive, intermediate, and combined (positive as well as intermediate images) datasets. The significant difference in results clearly show that independent models should be trained to classify positive and intermediate intensity images to achieve optimal performance. Overall results indicate that cell image classification for images pertaining to the intermediate intensity set is difficult as compared to the positive intensity images.
- Since number of samples of HEp-2 cell images are much larger in ICIP 2013 dataset as compared to MIVIA dataset, the classifiers are able to learn better and yield higher classification accuracies on ICIP 2013 database.

The results from Table 3.5 indicate that the performance results using different protocols vary significantly. The variation in results may be due to inability of classification algorithms to learn adequately when only few samples are available. Also, images in the dataset may not contain the adequate samples per class and therefore causing the effect of imbalance learning. Based on the results from this study, we find that the k-fold cross validation protocol may be preferred over leave-one-out cross validation protocol. The leave-one-out cross validation protocol in such cases only provides accuracy for one class which may not indicate the overall accuracy of the trained model. However, k-fold cross validation protocol provides the classification performance for all classes using equal proportions of data for each class. Therefore, it is our assertion that with 10 fold cross validation, texture features such Laws features with SVM or RDF classifiers can potentially provide a viable solution for HEp-2 cell image classification

3.5 Summary

This chapter discussed the emerging research efforts to develop computer aided systems for diagnosis of autoimmune diseases. Among various tasks in diagnosis of autoimmune diseases, the focus is to develop an efficient automated system for HEp-2 cell image classification. The existing research is analyzed based on a proposed feature categorization and the results reported on existing database. Laws texture features based system is proposed for the HEp-2 cell image classification. Experimental analysis is conducted using two public datasets and existing protocols. Results from comparative analysis concludes that the proposed system outperforms state-of-the-art techniques.

Table 3.5: Comparison results for all the baseline features using different protocols on MIVIA dataset. Overall cell classification accuracy values are reported for all feature and classifier combinations on the three protocols. On the lines of existing literature, all three protocols are applied on combined (both positive and intermediate) dataset.

Category	Feature	Classifier	Protocol 1	Protocol 2	10 fold CV
Geometric	Boundary	kNN	22.62	27.64	31.82
		RDF	28.34	31.03	52.64
		SVM-RBF	25.20	22.71	35.40
		SVM-Linear	26.43	27.19	28.11
	Shape & Size	kNN	29.70	27.03	35.87
		RDF	31.88	27.27	53.19
		SVM-RBF	32.70	28.21	41.44
		SVM-Linear	35.42	27.12	30.03
Texture	Gabor	kNN	27.11	22.44	49.21
		RDF	31.74	27.50	68.86
		SVM-RBF	27.11	33.72	67.97
		SVM-Linear	17.03	37.34	61.31
	RDWT	kNN	26.57	23.94	50.72
		RDF	27.79	22.45	66.59
		SVM-RBF	20.30	0.00	24.54
		SVM-Linear	20.30	14.29	14.23
	SGLD	kNN	27.25	20.23	40.06
		RDF	28.20	18.50	51.95
		SVM-RBF	35.42	24.54	55.74
		SVM-Linear	25.07	21.01	44.12
	GLRL	kNN	30.38	26.97	49.83
		RDF	32.29	30.53	70.37
		SVM-RBF	37.06	22.37	45.29
		SVM-Linear	33.92	28.98	41.79
	Laws	kNN	27.66	20.40	66.32
		RDF	23.84	19.17	**85.78**
		SVM-RBF	20.03	16.00	65.15
		SVM-Linear	48.37	42.25	70.31
Descriptor	LBP	kNN	30.52	25.01	72.24
		RDF	44.14	32.61	82.75
		SVM-RBF	**53.54**	40.88	82.13
		SVM-Linear	48.64	39.24	73.81
	HOG	kNN	40.60	34.29	62.74
		RDF	41.83	34.03	75.11
		SVM-RBF	45.50	42.47	80.21
		SVM-Linear	46.05	**46.49**	73.68
Others	Statistical	kNN	28.61	21.98	64.54
		RDF	37.19	22.97	73.34
		SVM-RBF	30.52	21.26	74.36
		SVM-Linear	45.23	31.47	49.35

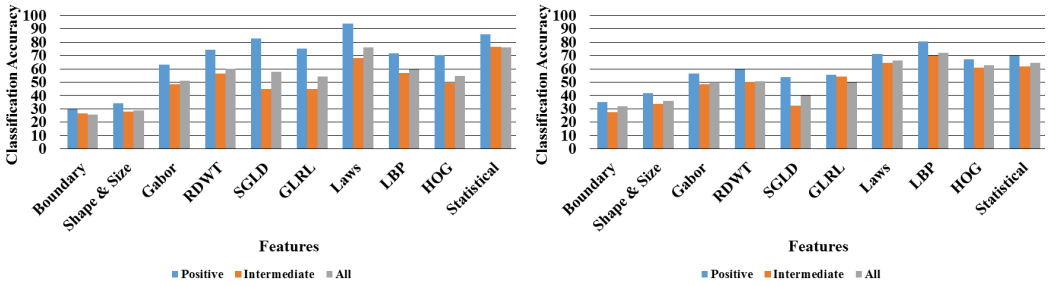

(a) k-Nearest Neighbour

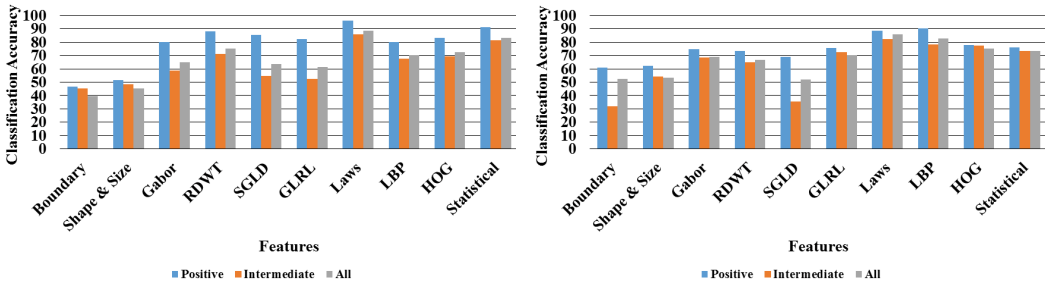

(b) Random Decision Forest

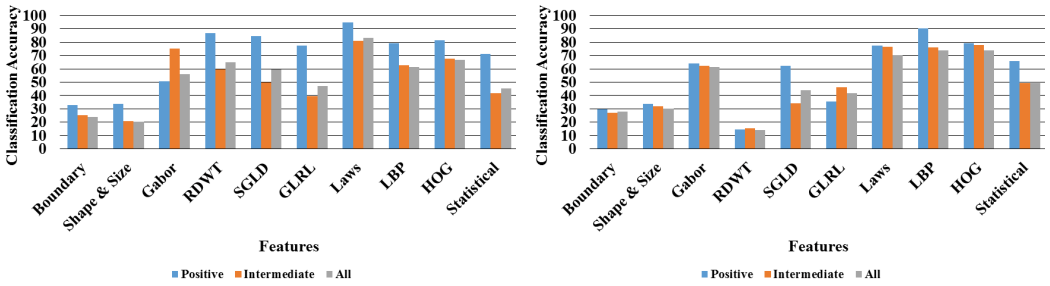

(c) SVM with linear kernel

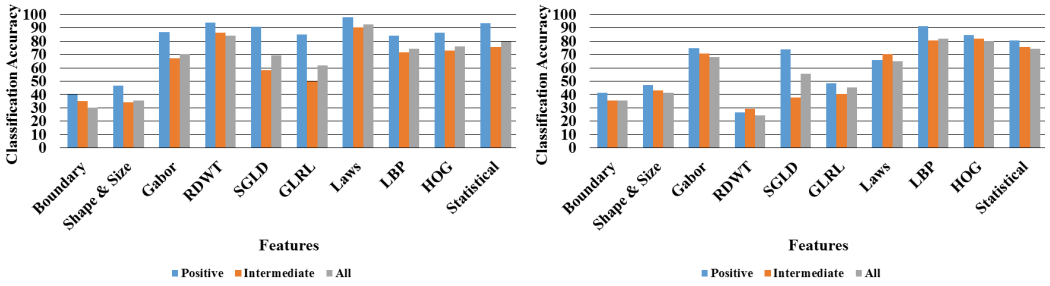

(d) SVM with RBF kernel

Figure 3.6: Comparison results using 10 fold cross validation on ICIP 2013 and MIVIA datasets. Left hand side graphs correspond to results on ICIP 2013 cell image classification contest training dataset [48] and the right hand side graphs present results on MIVIA dataset [32].

Chapter 4

Conclusion and Future Directions

In this thesis, we proposed computer aided systems to assist the screening of two dominant diseases among women - breast cancer and autoimmune diseases. To assist the clinicians in screening of breast cancer, a visual saliency based framework is proposed which detects potential mass locations in screening mammograms. The contributions of the proposed framework are two fold: (1) utilizing saliency maps for ROI segmentation and (2) classifying the regions into *mass* or *non-mass* classes using entropy features derived from both DWT and RDWT. We observe that unlike existing segmentation techniques, saliency approach does not require a prior step of pectoral muscle removal and can provide better segmentation. The segmented regions are analyzed in a grid based approach using different feature sets (e.g. texture, spatial, frequency, and wavelet) to detect masses via SVM classification. The detailed feature analysis, including feature selection approaches, suggests that entropy features derived from both DWT and RDWT yield the maximum classification accuracy. Based on the results from this research, we conclude that a visual saliency algorithm trained specifically to detect symptoms from screening mammograms would produce better results in the proposed framework. Clinical studies need to be performed to establish the key properties of such a visual saliency algorithm. Further efforts would be required to model the findings of these studies into an efficient algorithm.

In order to improve the screening practices of autoimmune diseases, we focus on the crucial HEp-2 cell image classification problem. We proposed to use Laws texture features for identification of antigen patterns from HEp-2 cell images. The effectiveness of Laws texture features is presented with the help of thorough experimental analysis. To facilitate a meaningful comparison, a feature categorization based on the object based properties of a cell image is proposed. The experimental analysis concludes that among various properties the features derived using the intensity patterns within the cell image are most efficient. Among various intensity based features, Laws texture features show high performance for the HEp-2 cell image classification on both the datasets. Two key insights of this research are: 1) HEp-2 cell image classification algorithms should consider the difference in image based properties of positive and intermediate category images for better performance and 2) more datasets with large number of images such as ICIP 2013 Cell Image Competition dataset are essential to adequately learn the automated models for complex HEp-2 cell image classification task. HEp-2 cell image classification is a relatively new area of research and based on our analysis of the existing literature, following research gaps need to be

addressed:

- Independent efforts have been made to automate individual modules of the complete automated analysis (presented in Figure 3.1). Future research should focus to completely automate the entire process.
- Efficient protocols based on practices in pattern recognition community, such as 10 fold cross validation, should be adopted to perform evaluation of proposed techniques in a more generic manner.
- More public datasets with large number of sample images would be helpful in substantial evaluation of the proposed techniques.

Bibliography

[1] World Health Statistics. Tech. rep., World Health Organization (WHO), 2013. http://www.who.int/gho/publications/world_health_statistics/EN_WHS2013_Full.pdf?ua=1.

[2] AVRAHAM, T., AND LINDENBAUM, M. Esaliency (extended saliency): Meaningful attention using stochastic image modeling. *IEEE Transactions on Pattern Analysis and Machine Intelligence 32*, 4 (2010), 693–708.

[3] BELHUMEUR, P., HESPANHA, J., AND KRIEGMAN, D. Eigenfaces vs. Fisherfaces: Recognition Using Class Specific Linear Projection. *IEEE Transactions on Pattern Analysis and Machine Intelligence 19*, 7 (1997), 711–720.

[4] BERMAN, C. G. Recent advances in breast-specific imaging. *Cancer Control Journal of the Moffitt Cancer Center 14*, 4 (2007), 338–349.

[5] BIZZARO, N., ANTICO, A., PLATZGUMMER, S., TONUTTI, E., BASSETTI, D., PESENTE, F., TOZZOLI, R., TAMPOIA, M., AND VILLALTA, D. Automated antinuclear immunofluorescence antibody screening: A comparative study of six computer-aided diagnostic systems. *Autoimmunity Reviews 13*, 3 (2014), 292–298.

[6] BIZZARO, N., TOZZOLI, R., TONUTTI, E., PIAZZA, A., MANONI, F., GHIRARDELLO, A., BASSETTI, D., VILLALTA, D., PRADELLA, M., AND RIZZOTTI, P. Variability between methods to determine ANA, anti-dsDNA and anti-ENA autoantibodies: a collaborative study with the biomedical industry. *Journal of Immunological Methods 219*, 12 (1998), 99–107.

[7] BONROY, C., VERFAILLIE, C., SMITH, V., PERSIJN, L., DE WITTE, E., DE KEYSER, F., AND DEVREESE, K. Automated indirect immunofluorescence antinuclear antibody analysis is a standardized alternative for visual microscope interpretation. *Clinical Chemistry and Laboratory Medicine 51*, 9 (2013), 1–9.

[8] BORGES SAMPAIO, W., MORAES DINIZ, E., CORRÊA SILVA, A., CARDOSO DE PAIVA, A., AND GATTASS, M. Detection of masses in mammogram images using CNN, geostatistic functions and SVM. *Computers in Biology and Medicine 41*, 8 (2011), 653–664.

[9] BORJI, A., AND ITTI, L. State-of-the-Art in Visual Attention Modeling. *IEEE Transactions on Pattern Analysis and Machine Intelligence 35*, 1 (2013), 185–207.

[10] BORJI, A., SIHITE, D. N., AND ITTI, L. Quantitative Analysis of Human-Model Agreement in Visual Saliency Modeling: A Comparative Study. *IEEE Transactions on Image Processing 22*, 1 (2013), 55–69.

[11] BOUCHERON, L. E. *Object- and Spatial-Level Quantitative Analysis of Multispectral Histopathology Images for Detection and Characterization of Cancer*. PhD thesis, University of California, Santa Barbara, 2008.

[12] BRANDT, S., KAREMORE, G., KARSSEMEIJER, N., AND NIELSEN, M. An Anatomically Oriented Breast Coordinate System for Mammogram Analysis. *IEEE Transactions on Medical Imaging 30*, 10 (2011), 1841–1851.

[13] BREM, R. F., HOFFMEISTER, J. W., ZISMAN, G., DESIMIO, M. P., AND ROGERS, S. K. A computer-aided detection system for the evaluation of breast cancer by mammographic appearance and lesion size. *American Journal of Roentgenology 184*, 3 (2005), 893–896.

[14] BREM, R. F., RAPELYEA, J. A., ZISMAN, G., HOFFMEISTER, J. W., AND DESIMIO, M. P. Evaluation of breast cancer with a computer-aided detection system by mammographic appearance and histopathology. *Cancer 104*, 5 (2005), 931–935.

[15] BURT, P., AND ADELSON, E. The Laplacian Pyramid as a Compact Image Code. *IEEE Transactions on Communications 31*, 4 (1983), 532–540.

[16] CADY, B., AND CHUNG, M. Mammographic screening: no longer controversial. *American journal of clinical oncology 28*, 1 (2005), 1–4.

[17] CASTRO, C., AND GOURLEY, M. Diagnostic testing and interpretation of tests for autoimmunity. *Journal of Allergy and Clinical Immunology 125*, 2 (2010), 1–23.

[18] CATALDO, S. D., BOTTINO, A., ISLAM, I. U., VIEIRA, T. F., AND FICARRA, E. Subclass discriminant analysis of morphological and textural features for hep-2 staining pattern classification. *Pattern Recognition 47*, 7 (2014), 2389–2399.

[19] CHANG, C. C., AND LIN, C. J. LIBSVM: A library for support vector machines. *ACM Transactions on Intelligent Systems and Technology 2*, 3 (2011), 1–27.

[20] CHENG, H., SHI, X., MIN, R., HU, L., CAI, X., AND DU, H. Approaches for automated detection and classification of masses in mammograms. *Pattern Recognition 39*, 4 (2006), 646–668.

[21] COPPLE, S. S., GILES, S. R., JASKOWSKI, T. D., GARDINER, A. E., WILSON, A. M., AND HILL, H. R. Screening for IgG Antinuclear Autoantibodies by HEp-2 Indirect Fluorescent Antibody Assays and the Need for Standardization. *American Journal of Clinical Pathology 137*, 5 (2012), 825–830.

[22] CORDELLI, E., AND SODA, P. Color to grayscale staining pattern representation in IIF. In *Computer Based Medical Systems* (2011), pp. 1–6.

[23] CREEMERS, C., GUERTI, K., GEERTS, S., VAN COTTHEM, K., LEDDA, A., AND SPRUYT, V. HEp-2 Cell Pattern Segmentation for the Support of Autoimmune Disease Diagnosis. In *International Symposium on Applied Sciences in Biomedical and Communication Technologies* (2011), pp. 28:1–28:5.

[24] DALAL, N., AND TRIGGS, B. Histograms of oriented gradients for human detection. In *IEEE Conference on Computer Vision and Pattern Recognition* (2005), vol. 1, pp. 886–893.

[25] DOI, K. Computer-aided diagnosis in medical imaging: historical review, current status and future potential. *Computerized Medical Imaging and Graphics 31*, 4-5 (2007), 198–211.

[26] EGERER, K., ROGGENBUCK, D., HIEMANN, R., WEYER, M.-G., BÜTTNER, T., RADAU, B., KRAUSE, R., LEHMANN, B., FEIST, E., AND BURMESTER, G.-R. Automated evaluation of autoantibodies on human epithelial-2 cells as an approach to standardize cell-based immunofluorescence tests. *Arthritis Research & Therapy 12*, 2 (2010), R40.

[27] ELBISCHGER, P., GEERTS, S., SANDER, K., ZIERVOGEL-LUKAS, G., AND SINAH, P. Algorithmic framework for HEp-2 fluorescence pattern classification to aid auto-immune diseases diagnosis. In *IEEE International Symposium on Biomedical Imaging: From Nano to Macro* (2009), pp. 562–565.

[28] ELTONSY, N., TOURASSI, G., AND ELMAGHRABY, A. A Concentric Morphology Model for the Detection of Masses in Mammography. *IEEE Transactions on Medical Imaging 26*, 6 (2007), 880–889.

[29] FAIRWEATHER, D., FRISANCHO-KISS, S., AND ROSE, N. R. Sex differences in autoimmune disease from a pathological perspective. *The American Journal of Pathology 173*, 3 (2008), 600–609.

[30] FARAKI, M., HARANDI, M. T., WILIEM, A., AND LOVELL, B. C. Fisher tensors for classifying human epithelial cells. *Pattern Recognition 47*, 7 (2014), 2348–2359.

[31] FERRARI, R. J., RANGAYYAN, R. M., DESAUTELS, J. E. L., BORGES, R. A., AND FRÈRE, A. F. Automatic identification of the pectoral muscle in mammograms. *IEEE Transactions on Medical Imaging 23*, 2 (2004), 232–245.

[32] FOGGIA, P., PERCANNELLA, G., SODA, P., AND VENTO, M. Benchmarking HEp-2 Cells Classification Methods. *IEEE Transactions on Medical Imaging 32*, 10 (2013), 1878–1889.

[33] FOWLER, J. The redundant discrete wavelet transform and additive noise. *IEEE Signal Processing Letters 12*, 9 (2005), 629–632.

[34] FOWLER, J. E. The redundant discrete wavelet transform and additive noise. *IEEE Signal Processing Letters 12*, 9 (2005), 629–632.

[35] FRIEDMAN, J. H., BENTLEY, J. L., AND FINKEL, R. A. An algorithm for finding best matches in logarithmic expected time. *ACM Transactions on Mathematical Software 3*, 3 (1977), 209–226.

[36] FRITZLER, M. J. The antinuclear antibody test: last or lasting gasp? *Arthritis and Rheumatism 63*, 1 (2011), 19–22.

[37] GANESAN, K., ACHARYA, U., CHUA, C., MIN, L., ABRAHAM, K., AND NG, K.-H. Computer-Aided Breast Cancer Detection Using Mammograms: A Review. *IEEE Reviews in Biomedical Engineering 6* (2013), 77–98.

[38] GANESAN, K., ACHARYA, U. R., CHUA, K. C., MIN, L. C., AND ABRAHAM, K. T. Pectoral muscle segmentation: A review. *Computer Methods and Programs in Biomedicine 110*, 1 (2013), 48–57.

[39] GAO, X., WANG, Y., LI, X., AND TAO, D. On Combining Morphological Component Analysis and Concentric Morphology Model for Mammographic Mass Detection. *IEEE Transactions on Information Technology in Biomedicine 14*, 2 (2010), 266–273.

[40] GIGER, M. L., CHAN, H.-P., AND BOONE, J. Anniversary Paper: History and status of CAD and quantitative image analysis: The role of Medical Physics and AAPM. *Medical Physics 35*, 12 (2008), 5799–5820.

[41] GONZALEZ, R. C., AND WOODS, R. E. *Digital Image Processing*, 2nd ed. 1992.

[42] HALKIOTIS, S., BOTSIS, T., AND RANGOUSSI, M. Automatic detection of clustered microcalcifications in digital mammograms using mathematical morphology and neural networks. *Signal Processing 87*, 7 (2007), 1559–1568.

[43] HARALICK, R. M., SHANMUGAM, K., AND DINSTEIN, I. Textural Features for Image Classification. *IEEE Transactions on Systems, Man and Cybernetics*, 6 (1973), 610–621.

[44] HAREL, J., KOCH, C., AND PERONA, P. Graph-based visual saliency. In *Advances in Neural Information Processing Systems* (2007), vol. 19, pp. 545–552.

[45] HEATH, M., BOWYER, K., KOPANS, D., KEGELMEYER JR, P., MOORE, R., CHANG, K., AND MUNISHKUMARAN, S. Current status of the Digital Database for Screening Mammography. In *International Workshop on Digital Mammography*. 1998, pp. 457–460.

[46] HIEMANN, R., HILGER, N., MICHEL, J., NITSCHKE, J., BÖHM, A., ANDERER, U., WEIGERT, M., AND SACK, U. Automatic analysis of immunofluorescence patterns of HEp-2 cells. *Annals of the New York Academy of Sciences 1109*, 1 (2007), 358–371.

[47] HO, T. K. Random decision forests. In *IEEE International Conference on Document Analysis and Recognition* (1995), vol. 1, pp. 278–282.

[48] HOBSON, P., PERCANNELLA, G., VENTO, M., AND WILIEM, A. Competition on cells classification by fluorescent image analysis. In *International Conference on Image Processing* (2013). `http://nerone.diiie.unisa.it/contest-icip-2013/index.shtml`.

[49] HOBSON, P., PERCANNELLA, G., VENTO, M., AND WILIEM, A. Contest on performance evaluation of indirect immunofluorescence image analysis systems. In *International Conference on Pattern Recognition* (2014). http://i3a2014.unisa.it/?page_id=91.

[50] HONG, B. W., AND SOHN, B. S. Segmentation of regions of interest in mammograms in a topographic approach. *IEEE Transactions on Information Technology in Biomedicine 14*, 1 (2010), 129–139.

[51] HOU, X., AND ZHANG, L. Saliency detection: A spectral residual approach. In *IEEE Conference on Computer Vision and Pattern Recognition* (2007), pp. 1–8.

[52] HUANG, Y.-L., JAO, Y.-L., HSIEH, T.-Y., AND CHUNG, C.-W. Adaptive Automatic Segmentation of HEp-2 Cells in Indirect Immunofluorescence Images. In *IEEE International Conference on Sensor Networks, Ubiquitous, and Trustworthy Computing* (2008), pp. 418–422.

[53] KARSSEMEIJER, N., AND TE BRAKE, G. Detection of stellate distortions in mammograms. *IEEE Transactions on Medical Imaging 15*, 5 (1996), 611–619.

[54] KOM, G., TIEDEU, A., AND KOM, M. Automated detection of masses in mammograms by local adaptive thresholding. *Computers in Biology and Medicine 37*, 1 (2007), 37–48.

[55] KONG, X., LI, K., CAO, J., YANG, Q., AND WENYIN, L. Hep-2 cell pattern classification with discriminative dictionary learning. *Pattern Recognition 47*, 7 (2014), 2379–2388.

[56] KUS, P., AND KARAGOZ, I. Fully automated gradient based breast boundary detection for digitized X-ray mammograms. *Computers in Biology and Medicine 42*, 1 (2012), 75–82.

[57] KWOK, S., CHANDRASEKHAR, R., AND ATTIKIOUZEL, Y. Automatic pectoral muscle segmentation on mammograms by straight line estimation and cliff detection. In *Intelligent Information Systems Conference* (2001), pp. 67–72.

[58] LAI, S., LI, X., AND BISCOF, W. On techniques for detecting circumscribed masses in mammograms. *IEEE Transactions on Medical Imaging 8*, 4 (1989), 377–386.

[59] LAWS, K. I. *Textured Image Segmentation*. PhD thesis, University of Southern California, 1980.

[60] LEVIN, D. A., PERES, Y., AND WILMER, E. L. *Markov Chains and Mixing Times*. American Mathematical Society, 2009.

[61] LI, H. D., KALLERGI, M., CLARKE, L. P., JAIN, V. K., AND CLARK, R. A. Markov random field for tumor detection in digital mammography. *IEEE Transactions on Medical Imaging 14*, 3 (1995), 565–576.

[62] LIU, L., AND WANG, L. Hep-2 cell image classification with multiple linear descriptors. *Pattern Recognition 47*, 7 (2014), 2400–2408.

[63] LIU, T., YUAN, Z., SUN, J., WANG, J., ZHENG, N., TANG, X., AND SHUM, H.-Y. Learning to Detect a Salient Object. *IEEE Transactions on Pattern Analysis and Machine Intelligence 33*, 2 (2011), 353–367.

[64] LOWE, D. G. Distinctive Image Features from Scale-Invariant Keypoints. *International Journal of Computer Vision 60*, 2 (2004), 91–110.

[65] MENCATTINI, A., RABOTTINO, G., SALMERI, M., AND LOJACONO, R. Assessment of a Breast Mass Identification Procedure Using an Iris Detector. *IEEE Transactions on Instrumentation and Measurement 59*, 10 (2010), 2505–2512.

[66] MERONI, P. L., AND SCHUR, P. H. ANA screening: an old test with new recommendations. *Annals of the Rheumatic Diseases 69*, 8 (2010), 1420–1422.

[67] MUSTRA, M., AND GRGIC, M. Robust automatic breast and pectoral muscle segmentation from scanned mammograms. *Signal Processing 93*, 10 (2013), 2817–2827.

[68] NANNI, L., PACI, M., AND BRAHNAM, S. Indirect immunofluorescence image classification using texture descriptors. *Expert Systems with Applications 41*, 5 (2014), 2463–2471.

[69] NOSAKA, R., AND FUKUI, K. Hep-2 cell classification using rotation invariant co-occurrence among local binary patterns. *Pattern Recognition 47*, 7 (2014), 2428–2436.

[70] OJALA, T., PIETIKÄINEN, M., AND HARWOOD, D. A comparative study of texture measures with classification based on featured distributions. *Pattern Recognition 29*, 1 (1996), 51–59.

[71] OLIVER, A., FREIXENET, J., MARTÍ, J., PÉREZ, E., PONT, J., DENTON, E. R. E., AND ZWIGGELAAR, R. A review of automatic mass detection and segmentation in mammographic images. *Medical Image Analysis 14*, 2 (2010), 87–110.

[72] OTSU, N. A Threshold Selection Method from Gray-Level Histograms. *IEEE Transactions on Systems, Man, and Cybernetics 9*, 1 (1979), 62–66.

[73] PENG, H., LONG, F., AND DING, C. Feature selection based on mutual information criteria of max-dependency, max-relevance, and min-redundancy. *IEEE Transactions on Pattern Analysis and Machine Intelligence 27*, 8 (2005), 1226–1238.

[74] PERNER, P., PERNER, H., AND MÜLLER, B. Mining knowledge for HEp-2 cell image classification. *Artificial Intelligence in Medicine 26*, 1 (2002), 161–173.

[75] PETRICK, N., CHAN, H. P., SAHINER, B., AND WEI, D. An adaptive density-weighted contrast enhancement filter for mammographic breast mass detection. *IEEE Transactions on Medical Imaging 15*, 1 (1996), 59–67.

[76] PISANO, E. D., GATSONIS, C., HENDRICK, E., YAFFE, M., BAUM, J. K., ACHARYYA, S., CONANT, E. F., FAJARDO, L. L., BASSETT, L., D'ORSI, C., JONG, R., AND REBNER, M. Diagnostic Performance of Digital versus Film Mammography for Breast-Cancer Screening. *New England Journal of Medicine 353*, 17 (2005), 1773–1783.

[77] POLAKOWSKI, W. E., COURNOYER, D. A., ROGERS, S. K., DESIMIO, M. P., RUCK, D. W., HOFFMEISTER, J. W., AND RAINES, R. A. Computer-aided breast cancer detection and diagnosis of masses using Difference of Gaussians and derivative-based feature saliency. *IEEE Transactions on Medical Imaging 16*, 6 (1997), 811–819.

[78] PONOMAREV, G. V., ARLAZAROV, V. L., GELFAND, M. S., AND KAZANOV, M. D. Ana hep-2 cells image classification using number, size, shape and localization of targeted cell regions. *Pattern Recognition 47*, 7 (2014), 2360–2366.

[79] RAHMATI, P., ADLER, A., AND HAMARNEH, G. Mammography segmentation with maximum likelihood active contours. *Medical Image Analysis 16*, 6 (2012), 1167–1186.

[80] RANGAYYAN, R., AYRES, F., AND LEO DESAUTELS, J. A review of computer-aided diagnosis of breast cancer: Toward the detection of subtle signs. *Journal of the Franklin Institute 344* (2007), 312–348.

[81] RANGAYYAN, R., SHEN, L., SHEN, Y., DESAUTELS, J. E. L., BRYANT, H., TERRY, T., HORECZKO, N., AND ROSE, M. Improvement of sensitivity of breast cancer diagnosis with adaptive neighborhood contrast enhancement of mammograms. *IEEE Transactions on Information Technology in Biomedicine 1*, 3 (1997), 161–170.

[82] RIGON, A., BUZZULINI, F., SODA, P., ONOFRI, L., ARCARESE, L., IANNELLO, G., AND AFELTRA, A. Novel opportunities in automated classification of antinuclear antibodies on HEp-2 cells. *Autoimmunity Reviews 10*, 10 (2011), 647–652.

[83] RIGON, A., SODA, P., ZENNARO, D., IANNELLO, G., AND AFELTRA, A. Indirect Immunofluorescence in Autoimmune Diseases : Assessment of Digital Images for Diagnostic Purpose. *Cytometry. Part B: Clinical Cytometry 72*, 6 (2007), 472–477.

[84] RIOUX, J. D., AND ABBAS, A. K. Paths to understanding the genetic basis of autoimmune disease. *Nature 435*, 7042 (2005), 584–589.

[85] SATOH, M., CHAN, E. K. L., HO, L. A., ROSE, K. M., PARKS, C. G., COHN, R. D., JUSKO, T. A., WALKER, N. J., GERMOLEC, D. R., WHITT, I. Z., CROCKETT, P. W., PAULEY, B. A., CHAN, J. Y. F., ROSS, S. J., BIRNBAUM, L. S., ZELDIN, D. C., AND MILLER, F. W. Prevalence and sociodemographic correlates of antinuclear antibodies in the United States. *Arthritis and Rheumatism 64*, 7 (2012), 2319–2327.

[86] SENTHILKUMAR, B., AND UMAMAHESHWARI, G. A Review on Computer Aided Detection and Diagnosis - Towards the treatment of Breast Cancer. *European Journal of Scientific Research 52*, 4 (2011), 437–452.

[87] SHEN, L., LIN, J., WU, S., AND YU, S. Hep-2 image classification using intensity order pooling based features and bag of words. *Pattern Recognition 47*, 7 (2014), 2419–2427.

[88] SINGH, S., AND BOVIS, K. An evaluation of contrast enhancement techniques for mammographic breast masses. *IEEE Transactions on Information Technology in Biomedicine 9*, 1 (2005), 109–119.

[89] SNELL, V., CHRISTMAS, W., AND KITTLER, J. Hep-2 fluorescence pattern classification. *Pattern Recognition 47*, 7 (2014), 2338–2347.

[90] SODA, P., AND IANNELLO, G. Aggregation of classifiers for staining pattern recognition in antinuclear autoantibodies analysis. *IEEE Transactions on Information Technology in Biomedicine 13*, 3 (2009), 322–329.

[91] STOKLASA, R., MAJTNER, T., AND SVOBODA, D. Efficient k-nn based hep-2 cells classifier. *Pattern Recognition 47*, 7 (2014), 2409–2418.

[92] SUCKLING, J., PARKER, J., DANCE, D., ASTLEY, S., HUTT, I., BOGGIS, C., RICKETTS, I., STAMATAKIS, E., CERNEAZ, N., KOK, S., TAYLOR, P., BETAL, D., AND SAVAGE, J. The mammographic images analysis society digital mammogram database. *Experta Medica International Congress Series 1069* (1994), 375–378.

[93] TANG, J., RANGAYYAN, R. M., XU, J., EL NAQA, I., AND YANG, Y. Computer-aided detection and diagnosis of breast cancer with mammography: recent advances. *IEEE Transactions on Information Technology in Biomedicine 13*, 2 (2009), 236–251.

[94] TANG, X. Texture information in run-length matrices. *IEEE Transactions on Image Processing 7*, 11 (1998), 1602–1609.

[95] THEODORAKOPOULOS, I., KASTANIOTIS, D., ECONOMOU, G., AND FOTOPOULOS, S. Hep-2 cells classification via sparse representation of textural features fused into dissimilarity space. *Pattern Recognition 47*, 7 (2014), 2367–2378.

[96] VAPNIK, V. N. *Statistical Learning Theory*, 1st ed. 1998.

[97] VARELA, C., TAHOCES, P. G., MÉNDEZ, A. J., SOUTO, M., AND VIDAL, J. J. Computerized detection of breast masses in digitized mammograms. *Computers in Biology and Medicine 37*, 2 (2007), 214–226.

[98] VELIKOVA, M., LUCAS, P. J., SAMULSKI, M., AND KARSSEMEIJER, N. A probabilistic framework for image information fusion with an application to mammographic analysis. *Medical Image Analysis 16*, 4 (2012), 865–875.

[99] VYBORNY, C. J., AND GIGER, M. L. Computer vision and artificial intelligence in mammography. *American Journal of Roentgenology 162*, 3 (1994), 699–708.

[100] WANG, Y., GAO, X., AND LI, J. A Feature Analysis Approach to Mass Detection in Mammography Based on RF-SVM. In *International Conference on Image Processing* (2007), vol. 5, pp. 9–12.

[101] WILIEM, A., SANDERSON, C., WONG, Y., HOBSON, P., MINCHIN, R. F., AND LOVELL, B. C. Automatic classification of human epithelial type 2 cell indirect immunofluorescence images using cell pyramid matching. *Pattern Recognition 47*, 7 (2014), 2315–2324.

[102] YANG, Y., WILIEM, A., ALAVI, A., LOVELL, B. C., AND HOBSON, P. Visual learning and classification of human epithelial type 2 cell images through spontaneous activity patterns. *Pattern Recognition 47*, 7 (2014), 2325–2337.

Chapter 5

Appendices

5.1 Fourier Domain Features

Three high level features are calculated which represent energy at high, medium, and low frequencies (Eq. 5.1- 5.3), other 32 energies are extracted from entire frequency spectrum at intervals of 32 using Eq. 5.4.

$$FFTlow = \sum_{n=0}^{340} |FFT\_ROI(n)|^2 \tag{5.1}$$

$$FFTmed = \sum_{n=341}^{683} |FFT\_ROI(n)|^2 \tag{5.2}$$

$$FFThigh = \sum_{n=684}^{1023} |FFT\_ROI(n)|^2 \tag{5.3}$$

$$FFTh = \sum_{n=32\cdot h}^{32\cdot(h+1)-1} |FFT\_ROI(n)|^2, \text{ where } h = 0, 1, ..., 31 \tag{5.4}$$

5.2 Intensity Features

Mean Intensity: Mean Intensity corresponds to the mean value of pixels in region R [61].

$$m = \frac{1}{N} \sum_{(i,j)\in R} I(i,j) \tag{5.5}$$

Intensity Variation: Intensity variation corresponds to the standard deviation of pixels in region R [61].

$$var = \sqrt{\frac{1}{N}\sum(I(i,j)-m)^2}\text{ , where} \tag{5.6}$$

$$m = \frac{1}{N}\sum I(i,j) \tag{5.7}$$

where $I(i,j)$ represents the image pixel value at (i,j) location and N the number of points in R.

Mean Intensity Difference: Mean intensity difference is the difference between the mean intensity of pixels within the region R and the mean intensity of pixels in the neighborhood Ne [61]. The neighborhood Ne is defined as region obtained after subtracting circular region ci from square region $s2$:

$$Ne = s2 - ci \tag{5.8}$$

Skewness: Skewness measures the asymmetry among data around the sample mean. Skewness of the distribution formed by pixels of region R is defined as third standardized moment of the distribution:

$$s = \frac{E(x-\mu)^3}{\sigma^3} \tag{5.9}$$

Kurtosis: Kurtosis measures the robustness of the distribution towards outliers. Kurtosis of the distribution formed by pixels of region R is defined as fourth standardized moment of the distribution:

$$k = \frac{E(x-\mu)^4}{\sigma^4} \tag{5.10}$$

where μ and σ are mean and standard deviation of the distribution and $E(x)$ gives expectation of variable x.

5.3 Laws Texture Features

Laws [59] proposed three basic kernels [1 2 1], [−1 0 −1], [−1 2 −1] to represent texture information. Combinations of the three basic kernels further produce five kernels [1 4 6 4 1], [−1 0 2 0 −1], [1 −4 6 −4 1], [−1 −2 0 2 1], [−1 2 0 −2 1] that represent edges, ripples, waves, lines, and spots in a square region. Texture filters are generated from these kernels by multiplication of two same size kernels, as a result 9 filters of size 3×3 and 25 filters of size 5×5 can be formed. These 34 filters are convolved with the given image to obtain the texture maps. From these texture maps three statistical measures - mean, absolute mean, and standard deviation are computed as feature values. In total, 102 features are derived from the given image. Eight feature masks used to compute Laws texture features are illustrated in Figure 5.1.

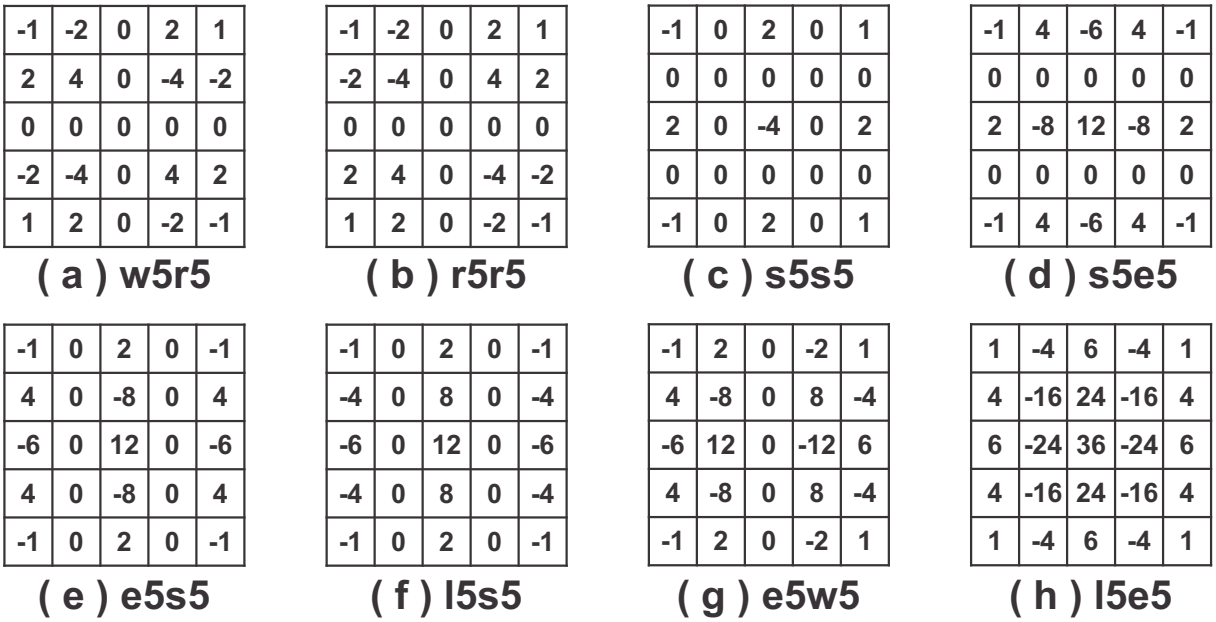

Figure 5.1: Feature masks generated using the kernels proposed by Laws [59].

5.4 Statistical Texture Features

Following equations define the notations helpful in describing features extracted from GLCM matrices,

$$C_x(i) = \sum_{j=1}^{N_g} C(i,j) \tag{5.11}$$

$$C_y(j) = \sum_{i=1}^{N_g} C(i,j) \tag{5.12}$$

$$C_{x+y}(k) = \sum_{\substack{i=1}}^{N_g} \sum_{\substack{j=1 \\ i+j=k}}^{N_g} C(i,j), k = 2,3,...,2N_g \tag{5.13}$$

$$C_{x-y}(k) = \sum_{\substack{i=1}}^{N_g} \sum_{\substack{j=1 \\ |i-j|=k}}^{N_g} C(i,j), k = 0,1,...,N_g - 1 \tag{5.14}$$

where N_g is the number of distinct gray levels, 8 in our case. With the help of notations defined above, 13 features are computed using the equations below:

- *Contrast or Inertia:*

$$f_1 = \sum_{n=0}^{N_g-1} n^2 \left\{ \sum_{\substack{i=1}}^{N_g} \sum_{\substack{j=1 \\ |i-j|=n}}^{N_g} C(i,j) \right\} \tag{5.15}$$

- *Correlation:*

$$f_2 = \frac{\sum_i \sum_j ijC(i,j) - \mu_x \mu_y}{\sigma_x \sigma_y} \tag{5.16}$$

where $\mu_x, \mu_y, \sigma_x, \sigma_y$ are the means and standard deviations of matrices C_x and C_y respectively.

- *Energy or Angular Second Moment:*

$$f_3 = \sum_i \sum_j C(i,j)^2 \tag{5.17}$$

- *Sum of squares:*

$$f_4 = \sum_i \sum_j (i-\mu)^2 C(i,j) \tag{5.18}$$

where μ is the mean of the GLCM matrix.

- *Entropy:*

$$f_5 = -\sum_i \sum_j C(i,j) log(C(i,j)) \tag{5.19}$$

- *Inverse Difference Moment:*

$$f_6 = \sum_i \sum_j \frac{1}{1+(i-j)^2} C(i,j) \tag{5.20}$$

- *Sum Average:*

$$f_7 = \sum_{k=2}^{2N_g} k C_{x+y}(k) \tag{5.21}$$

- *Sum Variance:*

$$f_8 = \sum_{k=2}^{2N_g} (k-f_7)^2 C_{x+y}(k) \tag{5.22}$$

- *Sum Entropy:*

$$f_9 = -\sum_{k=2}^{2N_g} C_{x+y}(k) log(C_{x+y}(k)) \tag{5.23}$$

- *Difference Variance:*

$$f_{10} = \sum_k (k-\mu_{x-y})^2 C_{x-y}(k) \tag{5.24}$$

where μ_{x-y} is the mean of C_{x-y}.

- *Difference Entropy:*

$$f_{11} = -\sum_{k=0}^{N_g-1} C_{x-y}(k) log(C_{x-y}(k)) \tag{5.25}$$

- *Information measures of Correlation:*

$$f_{12} = \frac{HXY - HXY_1}{max(HX, HY)} \tag{5.26}$$

$$f_{13} = [1 - e^{-2(HXY_2 - HXY)}]^{\frac{1}{2}} \tag{5.27}$$

$$HXY = -\sum_i \sum_j C(i,j) log(C(i,j)) \tag{5.28}$$

$$HX = -\sum_i C_x(i) log(C_x(i)) \tag{5.29}$$

$$HY = -\sum_j C_y(j) log(C_y(j)) \tag{5.30}$$

$$HXY_1 = -\sum_i \sum_j C(i,j) log(C_x(i) C_y(j)) \tag{5.31}$$

$$HXY_2 = -\sum_i \sum_j C_x(i) C_y(j) log(C_x(i) C_y(j)) \tag{5.32}$$

C is one of the four GLCM matrices, similar computations are made for all four matrices.

5.5 Run Length Texture Features

Run length distribution $r(j|\theta)$ and gray-level distribution $g(i|\theta)$ are derived from each of the four GLRL matrices $G(x, y|\theta)$ as,

$$r(j|\theta) = \sum_i G(i,j|\theta) \tag{5.33}$$

$$g(i|\theta) = \sum_j G(i,j|\theta) \tag{5.34}$$

The total number of runs in the image S are computed as,

$$S = \sum_i \sum_j G(i,j|\theta) \tag{5.35}$$

Following features are extracted from each of the four GLRL matrices using notations defined in Eq. 5.33-5.35,

- *Short Runs Emphasis (SRE):*

$$SRE = \frac{1}{S} \sum_j \frac{r(j|\theta)}{j^2} \tag{5.36}$$

- *Long Runs Emphasis (LRE):*

$$LRE = \frac{1}{S} \sum_j r(j|\theta) j^2 \tag{5.37}$$

- *Gray Level Non-uniformity (GLN):*

$$GLN = \frac{1}{S}\sum_{i} g(i|\theta)^2 \tag{5.38}$$

- *Run Length Non-uniformity (RLN):*

$$RLN = \frac{1}{S}\sum_{j} r(j|\theta)^2 \tag{5.39}$$

- *Run Percentage (RP):*

$$RP = \frac{1}{Area}\sum_{j} r(j|\theta) \tag{5.40}$$

where Area is the number of pixels in region R.